Chapter 2
Principles of Photoelectrochemical Cells

Roel van de Krol

2.1 The Photoelectrochemical Cell

Figure 2.1 shows a simplified energy diagram of a photoelectrochemical (PEC) cell based on a single photoanode and a metal counter electrode. More complicated configurations that involve photocathodes and/or more than one photoelectrode are discussed at the end of this chapter. The main component of the PEC cell is the semiconductor, which converts incident photons to electron–hole pairs. These electrons and holes are spatially separated from each other due to the presence of an electric field inside the semiconductor, the origin of which is discussed in Sect. 2.5. The photogenerated electrons are swept toward the conducting back-contact, and are transported to the metal counter-electrode via an external wire. At the metal, the electrons reduce water to form hydrogen gas. The photogenerated holes are swept toward the semiconductor/electrolyte interface, where they oxidize water to form oxygen gas.

For an alkaline electrolyte, the reduction and oxidation reactions can be written as[1]

$$4H_2O + 4e^- \rightleftarrows 2H_2 + 4OH^- \quad E^0_{red} = -0.828 \text{ V vs. NHE} \tag{2.1}$$

$$4OH^- + 4h^+ \rightleftarrows 2H_2O + O_2 \quad E^0_{ox} = -0.401 \text{ V vs. NHE.} \tag{2.2}$$

[1] Note that the sign of the potential for the oxidation half-reactions is opposite from that usually encountered in the literature, which usually lists these reactions as *reduction* reactions.

R. van de Krol (✉)
Faculty of Applied Sciences, Department Chemical Engineering/Materials for Energy Conversion and Storage, Delft University of Technology,
P.O. Box 5045, 2600 GA Delft, The Netherlands
e-mail: r.vandekrol@tudelft.nl

R. van de Krol and M. Grätzel (eds.), *Photoelectrochemical Hydrogen Production*, Electronic Materials: Science & Technology 102, DOI 10.1007/978-1-4614-1380-6_2,

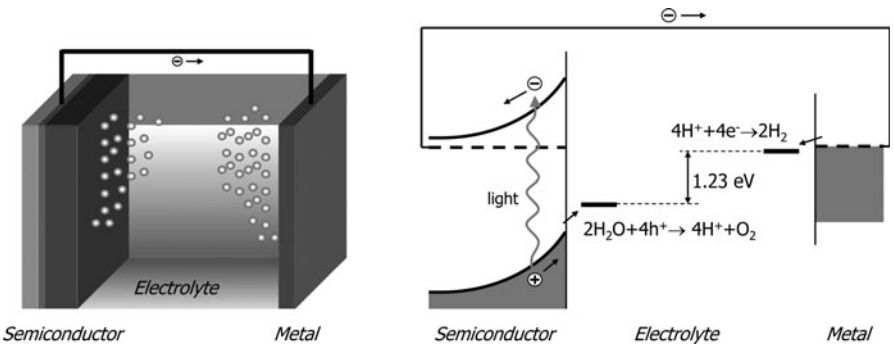

Fig. 2.1 Illustration of a photoelectrochemical cell that consists of a semiconducting photoanode and a metal cathode. The corresponding energy diagram is shown in the *right*

For an acidic environment, the appropriate reactions can be obtained from (2.1) and (2.2) by subtracting or adding the dissociation reaction of water into protons and hydroxyl ions:

$$4H^+ + 4e^- \rightleftarrows 2H_2 \quad E^0_{red} = +0.000 \text{ V vs. NHE} \tag{2.3}$$

$$2H_2O + 4h^+ \rightleftarrows 4H^+ + O_2 \quad E^0_{ox} = -1.229 \text{ V vs. NHE.} \tag{2.4}$$

The Gibbs free energy change for the overall water splitting reaction is given by the expression:

$$\Delta G = -nF\Delta E. \tag{2.5}$$

At standard temperature (298 K) and concentrations (1 mol/L, 1 bar), the electrochemical cell voltage ΔE of -1.229 V corresponds to a Gibbs free energy change of +237 kJ/mol H_2. This shows that the water-splitting reaction is thermodynamically *uphill*. This is markedly different from the photo*catalysis* reactions that one encounters in, e.g., photo-assisted degradation of organic pollutants, for which the Gibbs free energy change is negative.

2.2 Semiconducting Photoelectrode Materials

Some of the key requirements for a semiconductor photoelectrode are efficient absorption of visible light and good charge transport. It is often – though not always – easy to determine these parameters from an experiment on a particular material. Clearly, this approach becomes impractical if one wants to screen an entire class of candidate photoelectrode materials. For such cases a more fruitful

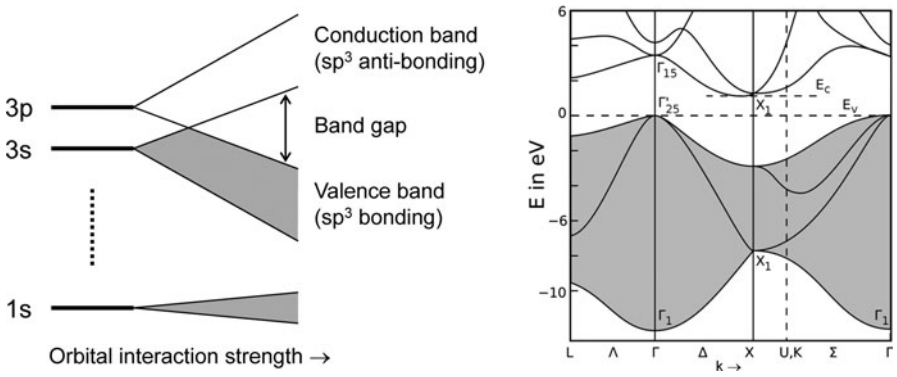

Fig. 2.2 *Left*: Formation of the valence and conduction bands in covalent semiconductors from bonding and antibonding sp^3 orbitals, respectively. *Right*: Calculated electronic band structure of silicon [1]. The *gray area* indicates occupied states in the valence band of the material

approach may be to calculate the electronic structure of a base material, and use this to predict how the properties depend on, e.g., composition. While still far from trivial, electronic structure calculations are now becoming more and more routine. The required computing power and software are readily available, and the number of electronic structure calculations reported in the literature, even by experimentally oriented groups, increases rapidly. However, in order to use these spectra to predict certain photoelectrode properties, one first needs to understand how chemical bonding between the atoms affects the electronic structure. Some of the main principles are discussed below. In contrast to most standard textbooks, we emphasize the properties of metal oxide semiconductors.

In most conventional semiconductors, such as Si and Ge, covalent bonding dominates. In silicon, for example, the outer 3s and 3p orbitals combine to form hybrid sp^3 orbitals. Neighboring sp^3 orbitals interact to form bonding and antibonding combinations that form the valence and conduction bands of the material, respectively. This is schematically illustrated in Fig. 2.2, which also shows the electronic band structure of silicon.

The bonding in metal oxide semiconductors is very different in nature. Since oxygen has a much higher electronegativity than any metal, the valence electrons are either fully or partially transferred from the oxygen to the metal ion. The bonding character of metal oxides is therefore highly polar or even ionic. A qualitative band picture can be obtained by constructing a molecular orbital (MO) diagram from the individual atomic energy levels. Figure 2.3 shows an example for rutile TiO_2, the very first and most extensively investigated photoanode material for water splitting [2, 3]. The main features of the MO diagram correspond quite well to the calculated band structure for rutile TiO_2, which is shown in Fig. 2.4. The valence band is mainly composed of O-2p orbitals, whereas the conduction band is primarily Ti-3d in character. One could think of the valence band as being occupied with the electrons that originally resided on the titanium

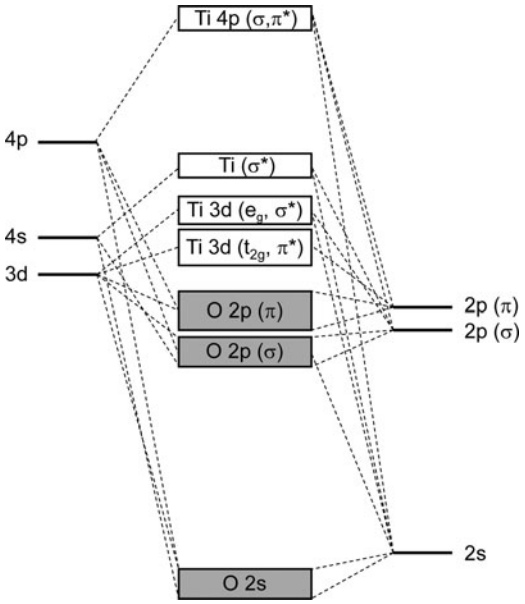

Fig. 2.3 Molecular orbital diagram of rutile TiO_2 (after Stoyanov [4] and Fisher [5])

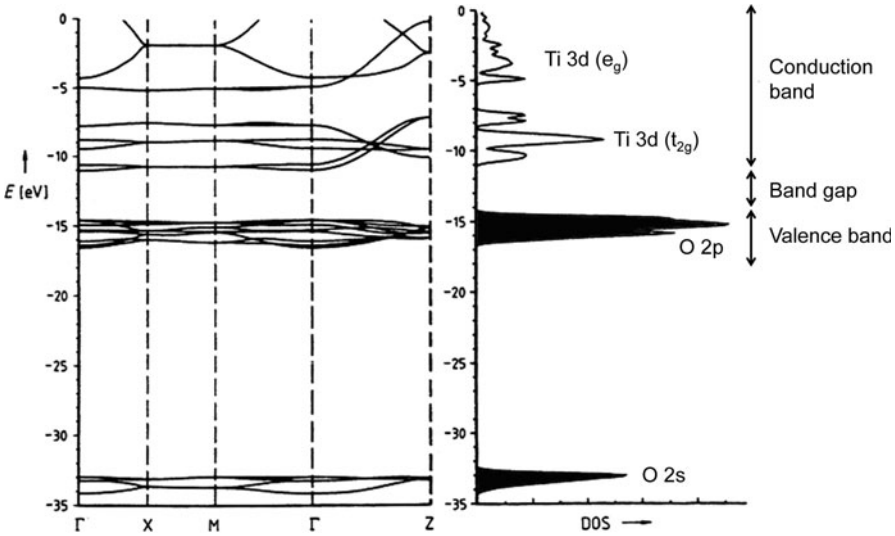

Fig. 2.4 Electronic band structure and density-of-states (DOS) of rutile TiO_2. The black parts of the DOS indicate completely filled bands. Adapted from Hoffmann [6], pp. 31, copyright Wiley-VCH Verlag GmbH & Co. KGaA. Reproduced with permission

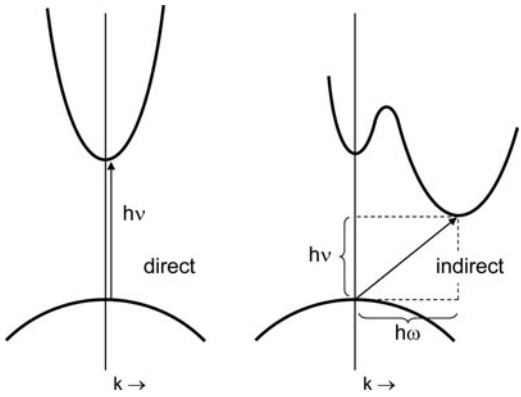

Fig. 2.5 Optical transitions in semiconductors with a direct and an indirect bandgap. The indirect transition requires assistance of a phonon with energy $h\omega$

atoms, before they were transferred to the more electronegative oxygen during the formation of the bond.[2]

It should be noted that such a "local" view is entirely inappropriate for covalent semiconductors such as silicon, in which the electrons are completely delocalized over the material. This local vs. delocalized view is a key feature that distinguishes metal oxide semiconductors from their covalently bonded counterparts. The local character of the energy bands in metal oxides sometimes leads to ambiguous interpretations. For example, "free" electrons in TiO_2 are sometimes distinguished from Ti^{3+} species. While such a distinction may be realistic at the surface of a material, where the electronic structure is distorted due to a disruption of the lattice symmetry, it is not obvious in the bulk in which the conduction band is mainly composed of Ti 3d orbitals.

While seemingly complicated, the electronic band structure can directly lead to several important insights for photoelectrode materials. The first insight is the nature of the optical transition, illustrated in more detail in Fig. 2.5. If the highest point in the valence band is located at the same *k*-vector as the lowest point of the conduction band, the optical transition does not require a change in crystal momentum. Such a transition is called *direct*, and is indicated by a vertical line in the *E*–*k* diagram. In contrast, *indirect* transitions do require a change in crystal momentum, as illustrated in Fig. 2.5. Since photons carry very little momentum, indirect transitions require absorption or emission of a phonon (i.e., a lattice vibration) and are much less likely to occur. As a consequence, the absorption coefficient of indirect semiconductors is much smaller than that of direct semiconductors – the difference can be two orders of magnitude. This is why direct semiconductors, such as amorphous Si or $CuIn_xGa_{1-x}Se_2$ (CIGS) can absorb all incident light in just a few micrometers, whereas crystalline (indirect) Si solar cells typically have a thickness

[2] The valence band of a semiconductor is analogous to the highest occupied molecular orbital (HOMO) in a molecule, whereas the conduction band is the solid state analogue of the lowest unoccupied molecular orbital (LUMO).

of ~300 μm. Metal oxides often have fairly horizontal-running *E-k* lines in their band structure (cf. Fig. 2.4), which sometimes obscures the direct vs. indirect nature.

The bandgap of a material can be determined from a measurement of the absorption coefficient vs. wavelength. If the bottom of the conduction band and the top of the valence band are assumed to have a parabolic shape, the absorption coefficient (units: m^{-1}) can be expressed as follows:

$$\alpha = \frac{A\left(h\nu - E_g\right)^m}{h\nu}. \tag{2.6}$$

Here, A is a constant and m depends on the nature of the optical transition: $m = ½$ for a direct bandgap, and $m = 2$ for an indirect gap. From (2.6), extrapolation of a plot of $(\alpha h\nu)^{1/2}$ vs. $h\nu$ plot gives the indirect bandgap, while a plot of $(\alpha h\nu)^2$ vs. $h\nu$ yields the direct bandgap of the material. Such a plot is called a "Tauc plot" [7] and is often encountered in the photoelectrochemistry and photocatalysis literature.

The second insight that can be obtained from the electronic band structure is the mobility of charge carriers, which is related to the width of the conduction and valence bands. For Si the bands are rather broad, spanning more than 10 eV. This is a direct consequence of the extensive overlap of the sp^3 orbitals on neighboring atoms. More overlap between atomic wavefunctions results in broader bands and easier transport of free charge carriers through the material. This can be quantified via the curvature of the individual bands, which is directly related to the effective mass and mobility of the charge carriers:

$$m^* = \frac{h^2}{\left(\frac{\partial^2 E}{\partial k^2}\right)} \quad \text{and} \quad \mu = \frac{q\tau}{m^*}. \tag{2.7}$$

Wide bands that are strongly curved indicate a high charge carrier mobility. A high mobility is especially desirable in photoelectrodes with an indirect bandgap. This is because these materials require a large thickness to absorb all the incident light, which means that photogenerated electrons and holes have to travel large distances before reaching the interface.

Table 2.1 gives an overview of the room temperature charge carrier mobilities of several semiconductors. What stands out are the small charge carrier mobilities for the transition metal oxides. One reason for this is the fact that the 3d orbitals in transition metals are fairly contracted, and show less overlap with neighboring atoms than the s- and p-orbitals. One can also look at this from an electrostatic point of view. The electrostatic interaction of a free electron with the cations surrounding it creates a local lattice distortion. This distortion accompanies the electron when it moves through the lattice, and is called a *polaron*. If the interaction is very strong, the polaron can even become trapped at a particular lattice site. The electron can then only move by thermally activated hopping, and its mobility will be very low. Similar considerations apply to "free" holes in the valence band, which can form polarons through electrostatic interaction with the surrounding oxygen ions. Charge transport via polarons is believed to play an important role in, e.g., hematite (α-Fe_2O_3), which will be discussed in more detail in Chap. 4.

Table 2.1 Charge carrier mobilities and effective masses at room temperature

	Mobility ($cm^2/V/s$)		Effective carrier masses ($\times m_e$)		
Material	Electrons	Holes	Electrons	Holes	References
Si	1,500	450			[8]
GaAs	8,500	400	0.07	0.68	[8, 9]
CdS	340	50	0.19	0.8	[8, 9]
ZnO	200	180	0.24	0.45	[8, 9]
TiO_2 (anatase)		2×10^{-3} [a]	>10	0.8	[10, 11]
WO_3	~10		~0.9		[12]
α-Fe_2O_3	0.1[b]	0.2[c]			[13]
p-Cu_2O		90			[14]
p-$CuAlO_2$		10			[15]
p-$SrCu_2O_2$		0.46			[16]
p-$CuMnO_2$		3.5×10^{-6}			[17]

[a]Theoretical estimate
[b]At 1,200 K
[c]At 1,400 K

The third piece of information that can be obtained from the electronic band structure is the density-of-states (DOS). This is the number of allowed electronic states per unit of energy interval. In E–k diagrams the k-values are equally spaced along the k-axis, so the DOS can be readily estimated from the total length of the black lines that run through a certain interval ΔE. As illustrated in Fig. 2.4 for TiO_2, the highest DOS occur at energies where the E–k curves are flat (horizontal). The DOS representation not only allows one to quickly and easily identify the various bands and band widths, but it also gives a rough impression of the optical transition probabilities between various bands. This is because the total number of excitations per second is proportional to the DOS at the occupied ground state (the initial state), multiplied by the transition probability to the final state, λ_{if}. The latter is given by Fermi's Golden Rule, (2.8), and depends linearly on the DOS at the final (excited) state, g_f:

$$\lambda_{if} = \frac{2\pi}{h} |M_{if}|^2 g_f. \tag{2.8}$$

In some cases, one can actually see certain features of the DOS reflected in the optical absorption spectrum of the material.

2.3 Charge Carriers and Doping

Under equilibrium conditions (i.e., no illumination and no net current flow), the concentration of free electrons in the conduction band and free holes in the valence band is given by the following expressions:

$$n = N_C \, e^{-(E_C - E_F)/kT} \quad \text{with} \quad N_C = 2\left(\frac{2\pi m_e^* kT}{h^2}\right)^{3/2}, \tag{2.9}$$

$$p = N_V \, e^{-(E_F - E_V)/kT} \quad \text{with} \quad N_V = 2\left(\frac{2\pi m_h^* kT}{h^2}\right)^{3/2}. \tag{2.10}$$

Equations (2.9) and (2.10) are valid for both undoped and doped semiconductors. They are, however, not valid when the Fermi level is less than ~3kT away from either one of the band edges. Under these conditions, the semiconductor is *degenerate*, and exhibits near-metallic behavior. The relationships for the effective densities of states were derived from the (nearly) free electron model, and may not be entirely accurate for transition metal oxides. Despite these limitations, (2.9) and (2.10) are exceedingly useful for describing the behavior of semiconducting photoelectrodes.

Semiconductors for practical applications are often doped, mainly with the aim to improve the conductivity. In metal oxide photoelectrodes, shallow donors and acceptors are almost always necessary because of the low intrinsic charge carrier mobilities. The conductivity of the material is given by $\sigma = ne\mu_e + pe\mu_h$, so increasing n or p will compensate for a small value of μ_e or μ_h. Examples of donor-type dopants are Ti^{4+} on a Fe^{3+} site in Fe_2O_3, or phosphorus in silicon. The extra valence electron introduced by the donor atom is loosely bound to the donor nucleus, and can be excited to the conduction band where it then contributes to the conductivity. Conversely, holes in acceptor-type dopants can be excited to the valence band. Since a hole is equivalent to a missing electron, one can also picture this as an electron being excited from the valence band into the energy level of the acceptor species.

If the dopant level is within ~2kT of E_C or E_V, it will be (almost) fully ionized at room temperature – this is referred to as a *shallow* dopant. For *deep* donors and acceptors, the degree of ionization can be calculated with the following equations:

$$\frac{N_D^+}{N_D} = \frac{1}{1 + g_D \, e^{(E_F - E_D)/kT}} \quad \text{and} \quad \frac{N_A^-}{N_A} = \frac{1}{1 + g_A \, e^{(E_A - E_F)/kT}}. \tag{2.11}$$

Here, E_D and E_A are the donor and acceptor energies and g_A and g_D are the corresponding degeneracy factors that reflect the multiplicity of the energy state [18]. Under the assumption that $n = N_D^+$, the following useful expressions relate the free electron concentration directly to the position of the donor level in the bandgap [18]:

$$n = \frac{N_\zeta}{2}\left(\sqrt{1 + \frac{4N_D}{N_\zeta}} - 1\right) \quad \text{with} \quad N_\zeta = \left(\frac{N_c}{g_D}\right) e^{-(E_C - E_D)/kT} \tag{2.12}$$

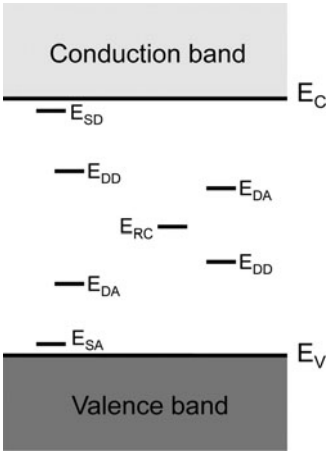

Fig. 2.6 Energy levels of shallow and deep donors (SD, DD) and acceptors (SA, DA) in a semiconductor. Deep donor or acceptor states can also occur below or above midgap, respectively. Midgap states (RC) are often very efficient recombination centers and can be either donor- or acceptor-like in nature

An analogous expression can be obtained for acceptor-doped materials. The energy levels for the various dopants are illustrated in Fig. 2.6. Deep dopants can act as optically active centers or as catalytically active surface sites, as given in the following paragraphs.

2.4 Defect Chemistry

Semiconducting photoelectrodes are almost always doped to improve their properties. In most cases, the aim is to enhance the n- or p-type conductivity, as described in Sect. 2.3. Certain dopants may enhance the optical absorption of wide bandgap semiconductors [19], increase the minority carrier diffusion length [20, 21], or enhance the catalytic activity at the surface of the semiconductor [22]. Other dopants adversely affect the properties, for example, by introducing midgap bulk or surface states that act as recombination centers [23, 24].

In addition to foreign cation and anion dopants, native point defects are also usually present in the material. Examples are vacancies, interstitials, or substituents.[3] These defects can have a similar influence on the optical, electrical, and catalytic properties as dopants. They are formed by intrinsic defect-chemical reactions, or by a change in the lattice stoichiometry due to exchange of, e.g., oxygen with the gas phase. Since virtually every defect affects the performance of the material in some way, the ability to understand and predict the relationship between dopants and defect concentrations is of paramount importance for designing efficient photoelectrodes.

[3] An example of a native substituent is a site exchange of A and B cations in a ternary compound such as AB_xO_y.

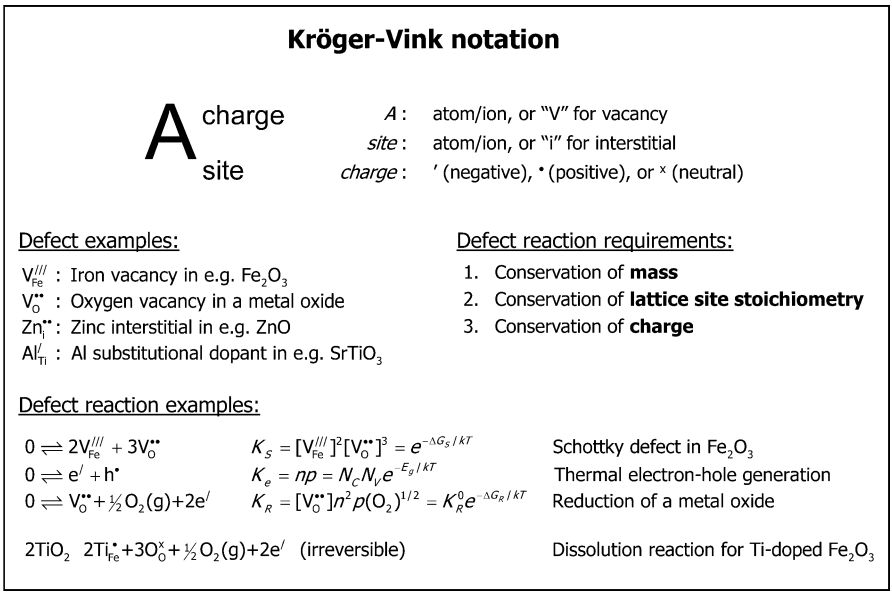

Fig. 2.7 Diagram summarizing the key elements of the Kröger–Vink notation for point defects in ionic solids. The formation of defects can be described with defect-chemical reactions and corresponding equilibrium constants

2.4.1 Doping Binary Metal Oxides

In covalently bonded semiconductors, the introduction of dopants is fairly straightforward since all lattice sites are similar to each other. This is even true for a polar compound such as GaAs. In this material, Si can be incorporated on both Ga and As lattice sites [25]. For ionically bonded materials the situation is quite different, since the large electrostatic penalty prevents any exchange of anions and cations. This puts certain restrictions on the incorporation of dopants, as given below.

The incorporation of dopants in metal oxides and other ionic materials can be conveniently described with the so-called *Kröger–Vink* notation [26], which is summarized in Fig. 2.7. For a more extensive description the reader is referred to several excellent textbooks on this subject [27, 28]. When describing defect-chemical reactions, one has to observe the conservation of mass and charge, just as one would for any other chemical (half)reaction. What is different in the defect chemistry of ionic solids is the *conservation of lattice site stoichiometry*. For example, if we dope Fe_2O_3 with zinc oxide, two zinc ions substitute for Fe, and the two oxygen ions occupy two of the three oxygen sites in the Fe_2O_3 unit. This means that the third oxygen site remains empty, resulting in an oxygen vacancy:

$$2ZnO \xrightarrow{Fe_2O_3} 2Zn_{Fe}^{'} + 2O_O^x + V_O^{\bullet\bullet}. \tag{2.13}$$

Note that this is an *irreversible* reaction, since spontaneous demixing will not occur. *This means that one cannot define an equilibrium constant for a dissolution reaction*. Closer inspection shows that reaction (2.13) indeed fulfills the required conservation of mass, charge, and lattice site stoichiometry.

One may try to get rid of the oxygen vacancy in reaction (2.13) by performing the synthesis in an oxygen-rich atmosphere. In this case, both mass and lattice site stoichiometry are conserved when adding the oxygen gas, which means that the charge has to be balanced by the addition of a hole:

$$2\mathrm{ZnO} + 1/2\mathrm{O_2(g)} \xrightarrow{\mathrm{Fe_2O_3}} 2\mathrm{Zn}'_{\mathrm{Fe}} + 3\mathrm{O}^{\mathrm{x}}_{\mathrm{O}} + \mathrm{h}^{\bullet}. \tag{2.14}$$

Note that the presence of a hole suggests p-type conductivity in Fe_2O_3. In many cases, however, metal oxides remain n-type when acceptor-doped. If this is the case, it is more appropriate to replace the hole with an electron on the left-hand side of (2.14).

In (2.13) and (2.14) the charge of the aliovalent[4] Zn dopant is compensated by an ionic defect ($V^{\bullet\bullet}_{O}$) and an electronic defect ($h^{\bullet}$), respectively. To illustrate the difference between these ionic and electronic compensation mechanisms in more detail, consider Ti-doped Fe_2O_3. When subtracting the ionic compensation reaction from the electronic one, we obtain

$$6\mathrm{TiO_2} \xrightarrow{3\mathrm{Fe_2O_3}} 6\mathrm{Ti}^{\bullet}_{\mathrm{Fe}} + 9\mathrm{O}^{\mathrm{x}}_{\mathrm{O}} + 3/2\mathrm{O_2(g)} + 6\mathrm{e}' \tag{2.15}$$

$$6\mathrm{TiO_2} \xrightarrow{4\mathrm{Fe_2O_3}} 6\mathrm{Ti}^{\bullet}_{\mathrm{Fe}} + 12\mathrm{O}^{\mathrm{x}}_{\mathrm{O}} + 2\mathrm{V}'''_{\mathrm{Fe}} \tag{2.16}$$

$$3\mathrm{O}^{\mathrm{x}}_{\mathrm{O}} + 2\mathrm{V}'''_{\mathrm{Fe}} \rightleftarrows 3/2\mathrm{O_2(g)} + 6\mathrm{e}'. \tag{2.17}$$

This shows that the difference between two *irreversible* dissolution reactions can be written as a *reversible* oxidation/reduction reaction. An important implication of this is that the addition of a dopant is, by itself, not sufficient to enhance the conductivity of a metal oxide photoelectrode: one also needs to ensure that the equilibrium of reaction (2.17) lies at the right-hand side. The factors that affect the equilibrium position are oxygen partial pressure, dopant concentration, and temperature. The equilibrium constant of (2.17) is given by

$$K = \frac{n^6 p_{\mathrm{O_2}}^{3/2}}{[\mathrm{V}'''_{\mathrm{Fe}}]^2}. \tag{2.18}$$

[4] An "aliovalent" dopant has different charge than the ion that it replaces.

From this, it is immediately clear that a low $p(O_2)$ favors electronic compensation. Moreover, K is constant, so at constant $p(O_2)$ the factor $n^6/[V_{Fe}^{'''}]^2$ also remains constant. This implies that at high dopant concentrations, ionic compensation will dominate over electronic compensation. In other words, a plot of the conductivity as a function of the Ti concentration will have its highest slope at low dopant concentrations. Finally, we note that the entropy (ΔS) of (2.17) strongly increases from left to right. Since $\Delta G = \Delta H - T\Delta S$, electronic compensation is favored at high temperatures.

It is interesting to note that after subtracting the Fe_2O_3 Schottky reaction (see Fig. 2.7) from (2.17), the standard oxygen reduction reaction for n-type oxides is obtained:

$$O_O^x \rightleftarrows V_O^{\bullet\bullet} + 1/2O_2(g) + 2e^{'}. \tag{2.19}$$

This reaction is of course valid for both doped and undoped metal oxides.

For doped metal oxides, the aliovalent metal ions influence the overall defect concentrations via what is sometimes called the "First Law of Doping." This law simply states that adding an aliovalent dopant increases the concentration of defects with opposite charges, and decreases the concentration of defects with charges of the same sign.

The concentration of dopants in metal oxides is usually limited to 1–2% at most, which corresponds to a concentration of ~10^{21} cm^{-3}. Higher concentrations are not likely to be effective, and may even lead to segregation of the dopant phase. If the conductivity of a doped metal oxide photoelectrode is found to be too low, it may be more effective to anneal it at high temperatures and under low $p(O_2)$ than to increase the dopant concentration.

In (2.13)–(2.16), only one type of ionic defect was considered for each ionic compensation reaction. In the case of ZnO-doped Fe_2O_3, the Zn acceptor could also be compensated by a cation interstitial ($Fe_i^{\bullet\bullet\bullet}$) instead of an oxygen vacancy. However, the higher charge of the interstitial Fe makes this energetically less favorable. Similarly, oxygen interstitials instead of iron vacancies could compensate the Ti donor in reaction (2.16), but in this case the large size of interstitial anions prohibits this.[5] In general, donor dopants are compensated by cation vacancies or electrons, while acceptor dopants are compensated by anion vacancies, cation interstitials, or holes. Which ionic defect is more likely to occur depends on the crystal structure, the ionic radius, and the charge of the ion.

[5] Anion interstitials normally only occur in oxides with the fluorite structure, which can be viewed as an fcc base lattice of cations in which the interstitial sites are occupied by anions.

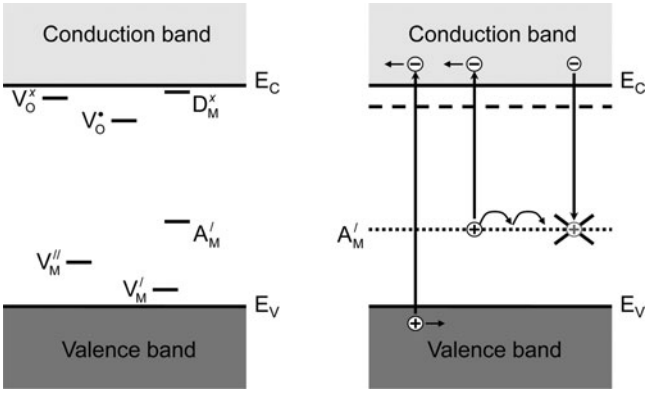

Fig. 2.8 *Left*: Energy diagram for a hypothetical a metal oxide, indicating several shallow and deep donor and acceptor levels. *Right*: n-Type oxide with optically active deep acceptor levels. After excitation, the holes have to hop to the interface via neighboring acceptor levels

2.4.2 Dopant Energy Levels

Most defects in metal oxides can have multiple oxidation states. For example, neutral oxygen vacancies can be ionized to divalent species in two steps:

$$V_O^x \rightleftarrows V_O^{\bullet} + e^{/} \tag{2.20}$$

$$V_O^{\bullet} \rightleftarrows V_O^{\bullet\bullet} + e^{/}. \tag{2.21}$$

The corresponding ionization energies are depicted in the energy diagram in the left-hand panel of Fig. 2.8. The common convention is to label the donor states by their charge *before* ionization, whereas acceptor states are labeled by their charge *after* ionization. Hence, D_M^x represents a shallow donor, and $A_M^{/}$ a deep acceptor.

As outlined above, shallow donors are used to increase the conductivity of an n-type oxide. Examples are Ti and Si in Fe_2O_3 [29–31], W in $BiVO_4$ [32], and Nb in TiO_2 [33]. Oxygen vacancies are often considered to be shallow donors as well, based on the observation that the conductivity of the oxide increases when reducing it at low $p(O_2)$. However, in many oxides – especially those with a fairly wide bandgap – the ionization energy of a singly ionized oxygen vacancy is simply too high ($>3\ kT$) to be considered as a shallow donor at room temperature. This implies that the conductivity is mostly determined by ionization of neutral oxygen vacancies, i.e., reaction (2.20). Note that this is somewhat different from the mechanism implied by reaction (2.19), in which reactions (2.20) and (2.21) are *both* assumed to occur. When present as deep

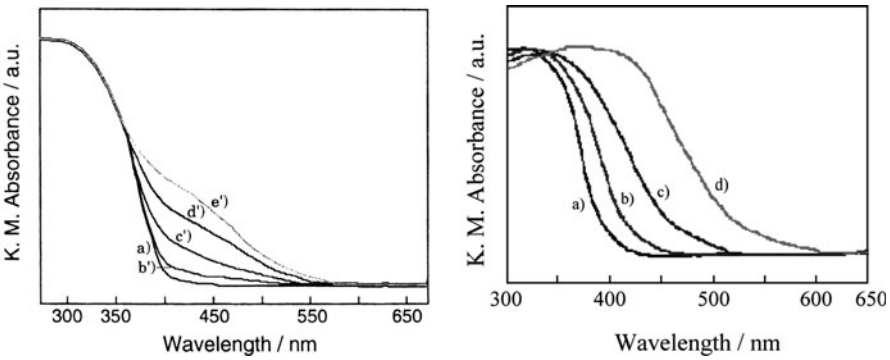

Fig. 2.9 *Left*: Optical absorption spectrum of TiO_2 doped with Cr via chemical impregnation. The amount of Cr increases from 0 wt% (**a**) to 1 wt% (**e′**). *Right*: Optical absorption of TiO_2 doped with Cr by physical implantation, with the Cr concentration increasing from 0 wt% (**a**) to 1.3 wt% (**d**). Reprinted from [34], with permission from Elsevier

donor species, ionized oxygen vacancies may adversely affect the performance of photoanodes by acting as recombination centers. If this is the case, their concentration can be kept low by doping with shallow donors, i.e., by using the First Law of Doping.

Cr and Fe are well-known examples of deep acceptors in TiO_2. As indicated in Fig. 2.8 (right), the electron in these acceptor levels can be optically excited to the conduction band. This requires less energy than the bandgap of the material, and Fe- and Cr-doped TiO_2 actually absorb visible light. An example of this is shown in Fig. 2.9 (left) for Cr-doped TiO_2. This visible light sensitization effect has attracted much interest in the field of photoelectrochemistry, especially in the late 1970s and early 1980s. A problem with this approach is that hole transport toward the interface is slow, as it takes place via hopping along neighboring acceptor levels (cf. Fig. 2.8). Moreover, the optical absorption cross section of these defects is small, requiring relatively thick films and long hole diffusion path lengths. Because of this, most holes recombine before reaching the interface. The photocurrents for Fe- or Cr-doped TiO_2 are indeed found to be low, and use of cation doping to improve the visible light absorption of wide-bandgap semiconductors has all but been abandoned in photoelectrochemistry. However, it still attracts interest in photocatalysis based on doped TiO_2 nanoparticles, where the holes only have to travel a short distance and recombination is less severe.

Interestingly, TiO_2 doped with Cr by physical ion implantation shows less recombination, and the shape of the absorption spectrum suggests an actual decrease of the bandgap instead of a local absorption center [34]. An example is shown in the right-hand side of Fig. 2.9. Clearly, the different incorporation methods for Cr give rise to different defects and a different electronic structure of the material. The physical reason for these differences remains to be established.

2.4.3 Defect Equilibria

If all the defect formation energies and/or equilibrium constants are known, the concentration of all the defects in a material can be calculated. As an example, we briefly consider the case for a hypothetical M_2O_3 photoanode doped with X^{4+}. Let us assume that X substitutes for the metal (as opposed to occupying an interstitial site), that Schottky disorder dominates in M_2O_3, and that the material is n-type ($n \gg p$). We furthermore assume that fully ionized oxygen vacancies are deep donors and can easily trap an electron, whereas singly ionized oxygen vacancies are shallow donors. We can then write the following defect equations and equilibrium constants:

$$2XO_2 \xrightarrow{M_2O_3} 2X_M^{\bullet} + 3O_O^{x} + 1/2O_2(g) + 2e^{/} \tag{2.22}$$

$$0 \rightleftarrows 3V_M^{///} + 2\,V_O^{\bullet\bullet} \quad K_S = [V_M^{///}]^3[V_O^{\bullet\bullet}]^2 \tag{2.23}$$

$$0 \rightleftarrows e^{/} + h^{\bullet} \quad K_e = np \tag{2.24}$$

$$O_O^{x} \rightleftarrows V_O^{\bullet\bullet} + 1/2O_2(g) + 2e^{/} \; K_R = n^2[V_O^{\bullet\bullet}]p_{O_2}^{1/2} \tag{2.25}$$

$$V_O^{\bullet} \rightleftarrows V_O^{\bullet\bullet} + e^{/} \; K_i = \frac{[V_O^{\bullet\bullet}]n}{[V_O^{\bullet}]}. \tag{2.26}$$

No equilibrium constant is defined for the dissolution reaction, since it is irreversible. Note that we have chosen to write the electronic compensation form of the dissolution reaction; we could have just as easily have chosen the ionic compensation reaction. As we saw before, they are related through reduction reaction (2.25) and are therefore not independent of each other.

We now have four equilibrium equations and five unknown variables ($[V_M^{///}]$, $[V_O^{\bullet\bullet}]$, $[V_O^{\bullet}]$, n, p). The missing equation is the electroneutrality equation:

$$3[V_M^{///}] + n = 2[V_O^{\bullet\bullet}] + [V_O^{\bullet}] + p \tag{2.27}$$

This system of nonlinear algebraic equations can be numerically solved with a computer, or one can find analytical solutions by simplification of (2.27) into six separate *Brouwer regimes*. Each Brouwer regime is characterized by a single dominant positive defect and a single dominant negative defect. While finding the right order of the different Brouwer regimes as a function of $p(O_2)$ may pose a bit of a challenge, one can derive all defect concentrations as a function of $p(O_2)$ by hand and plot these in a so-called "Brouwer diagram" (sometimes also

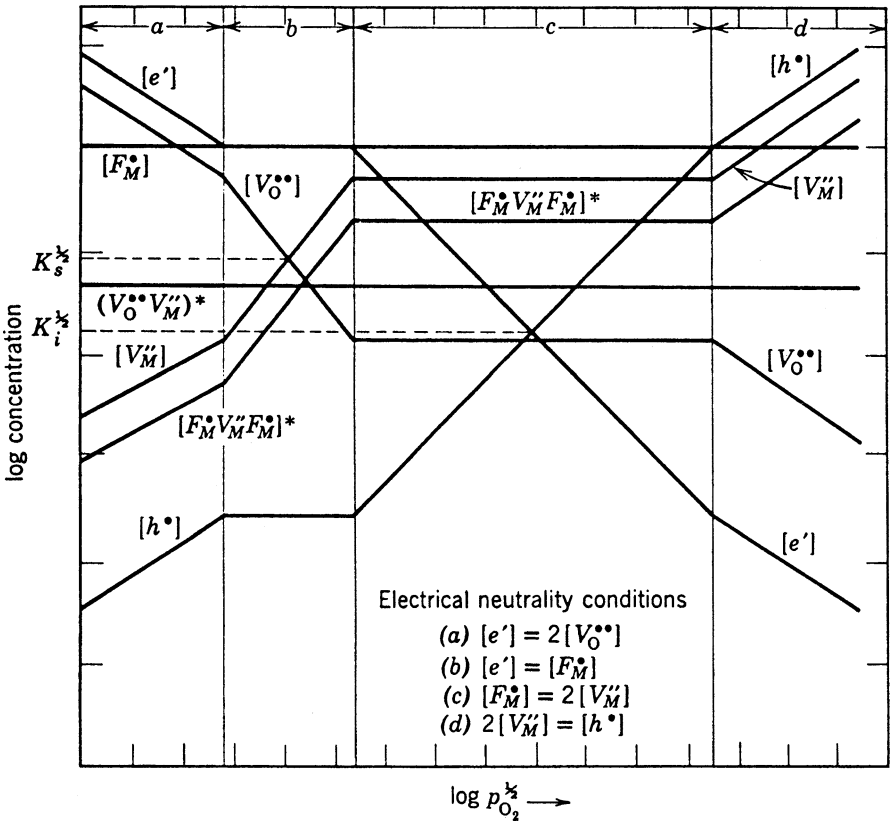

Fig. 2.10 Brouwer diagram for a metal oxide MO doped with a donor species (FO_2, with F being a metal ion) in which Schottky disorder dominates. Also indicated are defect associates (marked by an *asterisk*), clusters of defects that are held together by electrostatic forces. Such clusters are known to form at high defect concentrations. From [27], with permission

called a "Kröger–Vink diagram"). An example of such a diagram is shown in Fig. 2.10. Such diagrams can be very helpful in the study of metal oxide photoelectrodes since they immediately reveal which defects dominate in a certain $p(O_2)$ regime.

2.4.4 Doping of Complex Metal Oxides

Since only very few binary oxides show promise as photoelectrodes for water splitting, most notably WO_3 and Fe_2O_3, PEC research activities have now partly shifted toward ternary and more complex metal oxides (see, e.g., Chaps. 5 and 6). One of the best known examples is $BiVO_4$, which is an n-type semiconductor with a

bandgap of ~2.4 eV [35, 36]. Recent results from the author's laboratory show that electron transport limits the performance of undoped $BiVO_4$ photoanodes [32]. To improve this, one can dope $BiVO_4$ with tungsten in order to increase the concentration of free electrons. Tungsten has a valence of 6+ and a crystal ionic radius of 42 pm. It will therefore be a substitute for tetrahedrally coordinated V^{5+}, which has a slightly smaller ionic radius (36 pm).[6] When W^{6+} substitutes for V^{5+}, one might expect the positive charge to be compensated by free electrons, thereby increasing the conductivity. However, there is a minor complication: the compensating negative charge is already provided in the form of Bi vacancies. Since tungsten only occupies sites on the vanadium sublattice, the formation of Bi vacancies is necessary in order to preserve lattice site stoichiometry. This leads to the following electronic compensation reaction:

$$WO_3 + 1/2O_2(g) + 2e^{/} \xrightarrow{BiVO_4} V_{Bi}^{///} + W_V^{\bullet} + 4O_O^x. \qquad (2.28a)$$

According to (2.28a), W-doping actually *decreases* the conductivity of n-type $BiVO_4$, which is a rather unexpected (and undesired) result. It is also possible to write an alternative reaction in which lattice site stoichiometry is preserved by the segregation of vanadium out of the $BiVO_4$ in the form of V_2O_5:

$$2BiVO_4 + 2WO_3 \xrightarrow{2BiVO_4} 2Bi_{Bi}^x + 2W_V^{\bullet} + V_2O_5 + O_O^x + 1/2O_2(g) + 2e^{/}. \qquad (2.28b)$$

This avoids the need for highly charged cation vacancies, and the W dopant is now indeed charge-compensated by the desired free electrons. Which reaction actually occurs – (2.28a) or (2.28b) – depends on the energy required to form a triply charged Bi vacancy vs. the energy required to form a second phase.

It should be realized that reactions (2.28a) and (2.28b) are both unfavorable from an energetic point of view. In one case a highly charged defect has to be formed, while in the other case a second phase has to segregate out. This leads to an important general observation for ternary – and more complex – metal oxides: doping these materials by simply dissolving a binary oxide is difficult to achieve in practice. An elegant solution for this is to co-dope the $BiVO_4$ with equal amounts of W and Bi:

$$2WO_3 + Bi_2O_3 \xrightarrow{2BiVO_4} 2Bi_{Bi}^x + 2W_V^{\bullet} + 8O_O^x + {}^1/_2O_2(g) + 2e^{/}. \qquad (2.29)$$

Co-doping can be easily achieved by having a small excess of Bi over V during the synthesis of the material, so that [Bi] + [W] = [V]. This is a well known and powerful trick to increase the solubility of binary oxides in ternary oxides in order to incorporate donor- or acceptor-type dopants.

[6] Note that the octahedrally coordinated Bi sites (103 pm) are clearly too large for W, and would cause the W^{6+} to "rattle," which is energetically very unfavorable.

2.5 Space Charges and Band Bending

One of the key features of a semiconductor is the presence of a built-in electric field, or *space charge*. In devices for solar energy conversion, this field is responsible for the efficient separation of the photogenerated electrons and holes, thereby preventing recombination. The field is present near the surface or interface of a semiconductor, and is formed by the transfer of charges from the semiconductor bulk across its interface. The reason for charge transfer and the field induced by the remaining charges inside the semiconductor is described below.

2.5.1 Origin of the Space Charge Layer

In most semiconductor textbooks, the formation of a space charge is explained by a semiconductor being brought into contact with a metal or another semiconductor [8, 37]. When both materials have different Fermi levels (i.e., electrochemical potentials), charge is transferred between them until an equilibrium is established. In metal oxide semiconductors, a built-in electric field can even be formed at the surface without making contact with another solid. This is illustrated in the schematic diagram of Fig. 2.11. When a metal oxide is exposed to air, water molecules from the air can dissociatively adsorb at its surface, resulting in -OH surface termination. Since the symmetry of the bulk lattice is broken at the surface, these -OH groups form electronic surface states within the bandgap of the semiconductor. The energy levels of these surface states are below the conduction band minimum, and free electrons from the bulk will occupy these levels. The ionized donors from which the free electrons originated will of course stay behind in the bulk, where they form a positive space charge. An electric field now forms, and the charge transfer from bulk to surface will continue until the potential barrier becomes too large for bulk electrons to cross. At this point, a dynamic equilibrium establishes at which no net electron transport takes place. The Fermi level at the surface is then located somewhere halfway the DOS of the surface state.

2.5.2 Potential Distribution in The Depletion Layer

The potential distribution and width of space charge depend on the amount of charges transferred to the surface and the density of shallow donors in the material, N_D. Quantitative expressions for these relationships are indispensible in PEC research, and to understand where they come from, we derive them below. The geometry of the problem and the relevant parameters are schematically illustrated in Fig. 2.12. The starting point for the derivation is Poisson's law, which relates the potential to the net amount of charge:

$$\frac{d^2\phi}{dx^2} = \frac{-d\xi}{dx} = \frac{-\rho(x)}{\varepsilon_0 \varepsilon_r}. \tag{2.30}$$

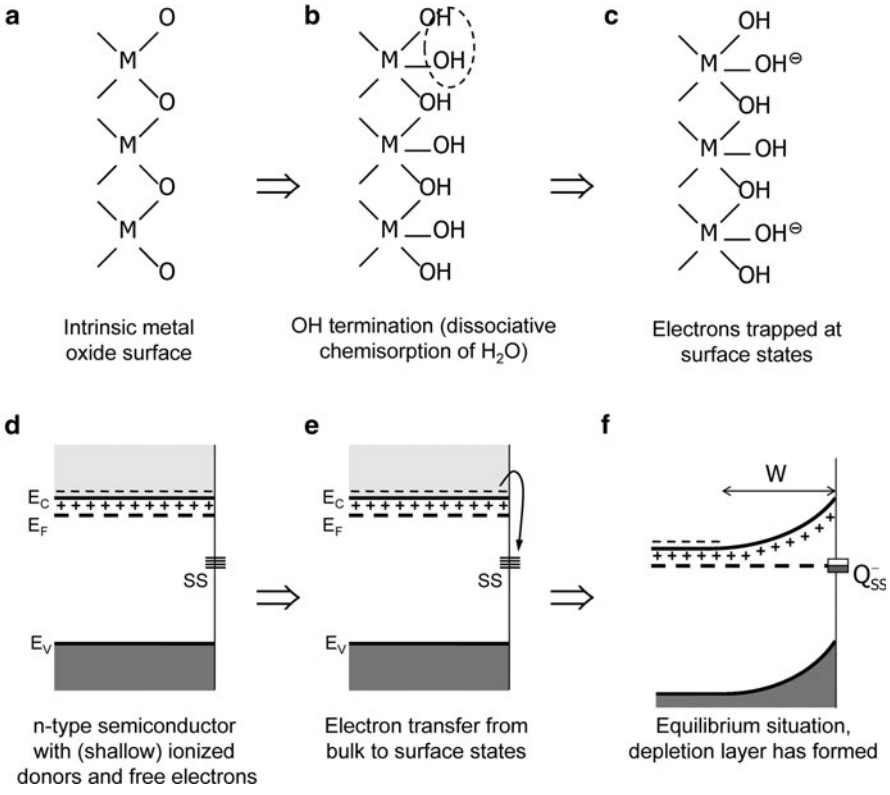

Fig. 2.11 Simplified illustration of the formation of a space charge region (SCR) at a metal oxide semiconductor surface when exposed to (humid) air

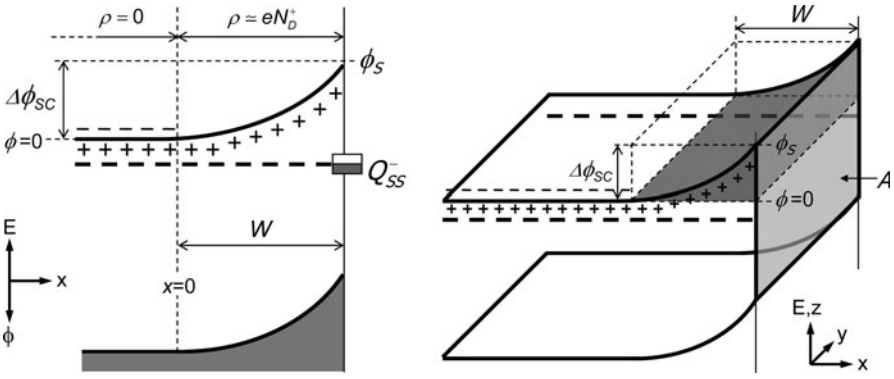

Fig. 2.12 Illustration of band bending at the surface of a n-type semiconductor in depletion. The "+" markers just below the conduction band represent the ionized donor species, whereas the "−" markers just above the conduction band level represent the free electrons. The potential in the bulk of the semiconductor is chosen as zero

Here, ξ was chosen as a symbol for the electric field to avoid confusion with symbol E for energy. The total charge density in the space charge is given by the concentration of free electrons, n, plus the concentration of ionized donors, N_D^+:

$$\rho(x) = \mathrm{e}\left(N_D^+ - n\right). \tag{2.31}$$

The concentration of free electrons is given by the distance between the conduction band minimum and the Fermi level, cf. (2.9). Inside the SCR, this distance is modified by the band bending $\phi(x)$, which leads to the following expression for n:

$$n(x) = N_C\,\mathrm{e}^{-(E_C - E_F - e\phi(x))/kT} = n_b\,\mathrm{e}^{e\phi(x)/kT}. \tag{2.32}$$

Note that the energy of an electron is related to its potential by $E = -e\phi$ and that the potential in the bulk of the semiconductor is conveniently chosen as zero (see Fig. 2.12). Since the bulk is electrically neutral, its electron concentration, n_b, must be equal to the number of ionized donors. The latter are assumed to be fully ionized, so that $N_D^+ = N_D = n_b$. Combining this with (2.31) and (2.32), the total charge density at point x can be written as

$$\rho(x) = eN_D\left(1 - \mathrm{e}^{e\phi(x)/kT}\right). \tag{2.33}$$

The combination of (2.30) and (2.33) cannot be readily solved due to the implicit dependence on $\phi(x)$. Fortunately, there is an elegant way around this by taking the derivative of the square of the electric field [38]. Using this with (2.30) yields:

$$\frac{\mathrm{d}\left(\xi^2\right)}{\mathrm{d}x} = 2\xi\frac{\mathrm{d}\xi}{\mathrm{d}x} = 2\xi\frac{\rho(x)}{\varepsilon_0\varepsilon_r} = -2\frac{\rho(x)}{\varepsilon_0\varepsilon_r}\frac{\mathrm{d}\phi}{\mathrm{d}x}. \tag{2.34}$$

Since there is a one-to-one correspondence between ϕ and x, we can now switch the independent variable from x to ϕ and rewrite (2.34) as

$$\xi^2 = \int_0^{\phi(x)} -2\frac{\rho(\phi)}{\varepsilon_0\varepsilon_r}\,\mathrm{d}\phi. \tag{2.35}$$

The total net charge between the (neutral) bulk and point x in the space charge can be related to the electric field at point x via the integral form of Gauss' law:

$$\xi = \frac{Q}{\varepsilon_0\varepsilon_r A}. \tag{2.36}$$

Here, A is the surface area of semiconductor. Combining (2.35) and (2.36) gives:

$$Q = \sqrt{-2\varepsilon_0\varepsilon_r A^2 \int_0^{\phi(x)} \rho(\phi)\,\mathrm{d}\phi}. \tag{2.37}$$

This equation provides a convenient starting point for further analysis of the space charge. It is generally applicable and can also deal with nonhomogeneous doping profiles and deep donors/acceptors. Here, we limit ourselves to homogeneously distributed shallow donors, for which the charge density is given by (2.33).

The total amount of charge in the SCR can now be obtained by combining (2.33) and (2.37) and integrating between $\phi = 0$ and $\phi = \phi_S = -\phi_{SC}$:

$$\begin{aligned} Q_{SC} &= \sqrt{-2\varepsilon_0\varepsilon_r A^2 \int_0^{-\phi_{sc}} eN_D(1 - \mathrm{e}^{e\phi/kT})\,\mathrm{d}\phi} \\ &= \sqrt{2\varepsilon_0\varepsilon_r eN_D A^2 \left(\phi_{SC} + \frac{kT}{e}\,\mathrm{e}^{-e\phi_{SC}/kT} - \frac{kT}{e}\right)}. \end{aligned} \tag{2.38}$$

Under normal PEC operating conditions, the potential drop across the space charge is at least 0.1 V, and the previous result can be simplified to

$$Q_{SC} = \sqrt{2\varepsilon_0\varepsilon_r eN_D A^2 \left(\phi_{SC} - \frac{kT}{e}\right)}. \tag{2.39}$$

The total amount of charge is related to the depletion layer thickness via

$$Q_{SC} = eN_D AW \tag{2.40}$$

which leads to the following widely used expression for the space charge width:

$$W = \sqrt{\frac{2\varepsilon_0\varepsilon_r}{eN_D}\left(\phi_{SC} - \frac{kT}{e}\right)}. \tag{2.41}$$

Although this important result was derived for n-type semiconductors, it is also valid for p-type materials if N_D is replaced with the shallow acceptor density, N_A.

To get an idea of typical numbers, Fig. 2.13 shows the calculated depletion layer width for α-Fe_2O_3 as a function of ϕ_{SC} for various dopant densities. Typical values range between 5 and 500 nm. The total amount of charge in the depletion layer has to be compensated by a sheet of oppositely charged species (e.g., trapped electrons) at the surface of the material. As can be seen in the right-hand part of Fig. 2.13, less

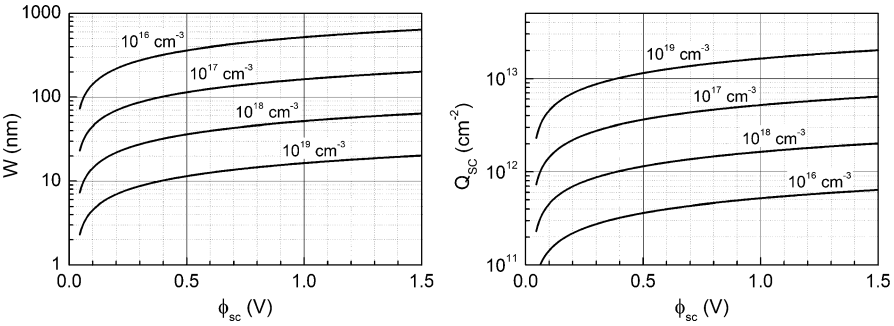

Fig. 2.13 *Left*: Depletion layer width as a function of potential drop across the space charge (ϕ_{SC}) and (shallow) dopant density. *Right*: Corresponding amount of adsorbed surface charges needed to compensate the charges in the depletion layer. The data are calculated for α-Fe_2O_3 assuming a static dielectric constant of 25 [39, 40]

than 1% of a monolayer[7] of adsorbed surface charges is already more than sufficient to induce a significant space charge layer in the material.

The actual values of the dopant density and the depletion layer width can be determined by impedance measurements. Under certain conditions one can extract the differential capacitance of the space charge, C_{SC}, from the total impedance of the system. C_{SC} can be derived by differentiating (2.39) with respect to ϕ_{SC}:

$$\frac{1}{C_{SC}^2} = \left(\frac{dQ_{SC}}{d\phi_{SC}}\right)^{-2} = \frac{2}{\varepsilon_0 \varepsilon_r e N_D A^2}\left(\phi_{SC} - \frac{kT}{e}\right). \tag{2.42}$$

This is the so-called "Mott–Schottky" equation. Typical values for C_{SC} are 10–1,000 nF/cm^2. By plotting $1/{C_{SC}}^2$ as a function of the applied potential, the donor density of the semiconductor can be determined.

2.5.3 Deep Depletion, Inversion, and Accumulation Layers

In addition to the depletion layer, other types of space charges can also form in a semiconductor. These are illustrated in Fig. 2.14. If the number of adsorbed negative (positive) surface charges increases beyond a certain number for an n-type (p-type) semiconductor, the Fermi level crosses the middle of the bandgap and the surface region becomes p-type (n-type). This is called an inversion layer. Formation of an inversion layer is not always possible; if the dominant charge carriers in the inversion layer are annihilated faster than they are (thermally)

[7] 1 monolayer (ML) corresponds to ~10^{15} atoms/cm^2.

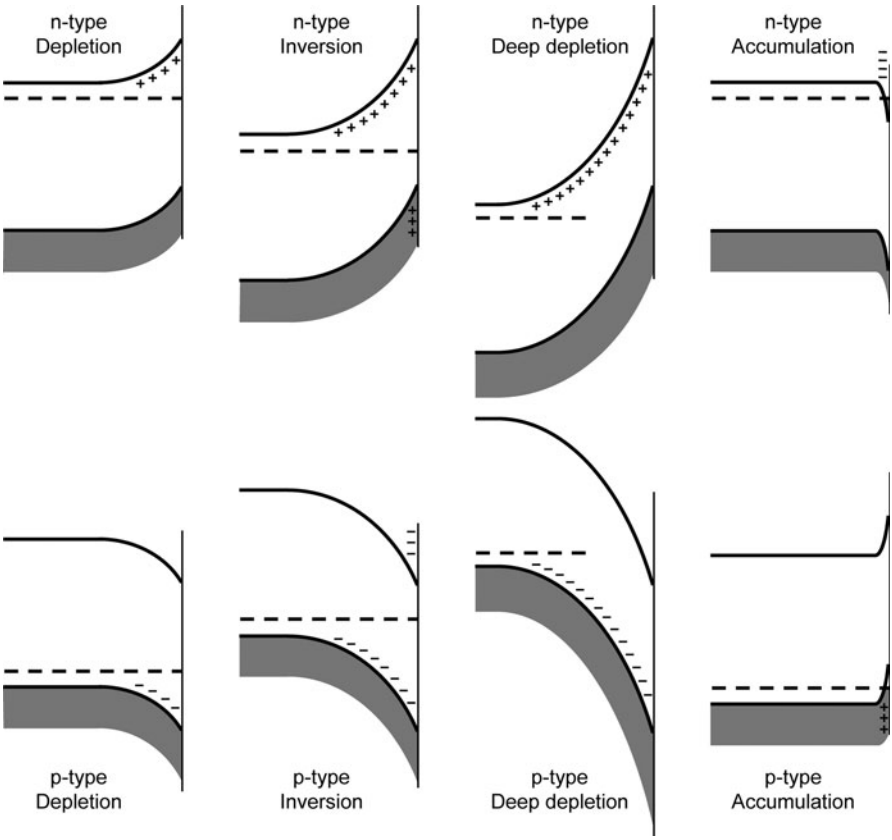

Fig. 2.14 Different types of space charges in n- and p-type semiconductors. A normal depletion layer contains only ionized donors or acceptors. An inversion layer is formed when the Fermi level crosses the midgap energy, and the minority carriers outnumber the majority carriers in a thin layer at the surface. When these minority carriers are consumed faster than they are generated, a deep depletion layer forms; under these conditions the surface is not in thermal equilibrium and the Fermi level is not well defined in this region. In an accumulation layer, the adsorbed surface charges are compensated by majority charge carriers that accumulate at the surface

generated, no free charge carriers are present and the surface remains insulating. A deep depletion layer is then formed. Deep depletion layers are fairly common in photoelectrode materials with a relatively large bandgap (>2 eV) because generation of minority carriers is difficult in these materials. They can also be formed in the presence of surface-adsorbed species that consume the minority carriers through fast oxidation or reduction reactions. An accumulation layer can form when an excess of positive (negative) charges is adsorbed at the surface of an n-type (p-type) semiconductor. To compensate these surface charges, free majority carriers will accumulate near the surface, forming the accumulation layer.

Whereas the charge density in a depletion layer is limited by the concentration of ionized dopant ions (usually 10^{16}–10^{18} cm^{-3}), the concentration of electronic

charge carriers is limited by the effective density of states and can reach values up to ~10^{20} cm^{-3}. Due to this high density, the widths of the accumulation layer and the thin inverted surface region for an inversion layer are usually in the order of 1–15 nm, i.e., much thinner than that of a typical depletion layer. The width of a deep depletion layer can be evaluated by the same expression as that for a normal depletion layer. The expressions for the thickness of the inversion and accumulation layers are seldom necessary in photoelectrochemical water splitting – they can be found in the literature [8, 41]. Finally, it should be noted that all four space charge layers can, in principle, be formed by applying an external potential to a semiconductor photoelectrode. The effect of applying a potential is discussed in the next section.

2.6 The Semiconductor–Liquid Junction

When a metal oxide semiconductor is exposed to humid air, hydroxylation of the surface occurs as described in Sect. 2.5.1. A slightly more complicated situation arises when the semiconductor is immersed in an aqueous solution. Depending on the pH of the solution, specific adsorption of protons and/or hydroxide species affect the charge distribution at the semiconductor/electrolyte interface, and thereby also the potential distribution. Analysis of the potential distribution allows us to construct an energy diagram of the complete PEC cell. This diagram is indispensible for a thorough understanding of the thermodynamics of PEC devices, as well as the charge transfer processes that make it work.

2.6.1 Surface Hydroxylation

When a semiconductor is immersed in an aqueous solution, H^+ and OH^- ions in the solution will continuously adsorb and desorb from the surface. A dynamic equilibrium will be established, which can be described by the following protonation and deprotonation reactions:

$$M - OH \underset{}{\overset{k_a}{\rightleftharpoons}} MO^- + H^+_{aq} \tag{2.43}$$

$$M - OH + H^+_{aq} \overset{k_b}{\rightleftharpoons} M - OH^+_2. \tag{2.44}$$

The equilibrium of these reactions depends on the pH of the solution and the Brønsted acidity of the surface. Depending on these conditions, the net total charge adsorbed at the surface will be positive, zero, or negative. The pH at which the net adsorbed charge is zero is called the point of zero charge (PZC) of the semiconductor.

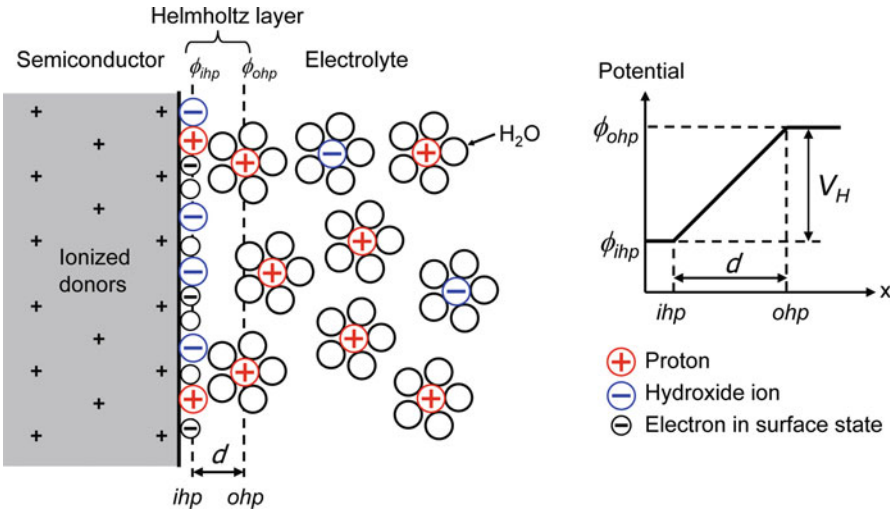

Fig. 2.15 Schematic model of the semiconductor/electrolyte interface and the Helmholtz layer. The inner Helmholtz plane (*ihp*) consists of H^+ and OH^- ions that are specifically adsorbed at the semiconductor surface. The outer Helmholtz plane (*ohp*) marks the distance of closest approach for ions still in the solution. The distance *d* is only a few Ångströms due to the solvation sheet of water molecules surrounding each ion

Note that the reactions (2.43) and (2.44) are only appropriate for hydroxylated semiconductor surfaces that are amphoteric,[8] which is indeed true for most metal oxide photoelectrodes.

2.6.2 The Semiconductor/Electrolyte Interface

The structure of the semiconductor/electrolyte interface is illustrated in Fig. 2.15. The charges at the surface consists of electrons (or holes) trapped in surface states, plus the specifically adsorbed ions described in reactions (2.43) and (2.44). The counter charges are provided by ionized donors or acceptors in the solid, plus an accumulation of oppositely charged ions in the solution. Due to the large dipole moment of water, all ions in the solution are surrounded by a solvation cloud of water molecules. This cloud prevents them from approaching the surface closer than a few Ångströms (see Fig. 2.15). The region between the specifically adsorbed ions and the closest ions in the solution is called the *Helmholtz layer*. The potential drop across this layer is given by

[8] "Amphoteric" means that the semiconductor surface can either donate or accept a proton, i.e., it can act both as a Brønsted acid and as a Brønsted base.

$$V_H = \xi d = \frac{Q_S d}{\varepsilon_0 \varepsilon_r}. \tag{2.45}$$

The width of the Helmholtz layer is ~2–5 Å, and on such a small length scale the dielectric constant of water is estimated to be ~6, i.e., much smaller than its bulk value of 80 [42]. For a surface charge of $Q_S = 10^{13}$ cm^{-2} (Fig. 2.13), the potential drop across the Helmholtz layer is typically in the order of ~0.1–0.5 V. The Helmholtz capacitance is 10–20 μF/cm^2 [42].

During adsorption and desorption from the semiconductor surface, the ions gain or lose energy while crossing the Helmholtz layer due to the Helmholtz voltage. This leads to the following equilibrium constants for reactions (2.43) and (2.44):

$$\frac{[M-O^-][H^+_{aq}]}{[M-OH]} = k_a = \exp\left(\frac{-(\Delta G_a - eV_H)}{kT}\right) \tag{2.46}$$

$$\frac{[M-OH_2^+]}{[M-OH][H^+_{aq}]} = k_b = \exp\left(\frac{-(\Delta G_b + eV_H)}{kT}\right). \tag{2.47}$$

Making use of the fact that $V_H = 0$ and [M–O$^-$] = [M–OH$_2^+$] at pH = PZC, the Gibbs free energies can be eliminated to yield the following expression for V_H:

$$V_H = \frac{2.3kT}{e} \log\left(\frac{[M-O^-]}{[M-OH_2^+]}\right)^{1/2} + \frac{2.3kT}{e}(PZC - pH). \tag{2.48}$$

As seen above, the excess charge at the surface is usually very small, in the order of 1% of a monolayer or less. Hence, [M–O$^-$] ≈ [M–OH$_2^+$] and (2.48) can be simplified to

$$V_H = \frac{2.3kT}{e}(PZC - pH). \tag{2.49}$$

This important result shows that the Helmholtz potential changes with -59 mV ($2.3kT/e$) per pH unit at 25°C.

2.6.3 The Band Diagram

Now we understand the structure of the semiconductor/electrolyte interface, we can draw a detailed band diagram for a complete PEC cell. An example is shown in Fig. 2.16 for a cell composed of a n-type photoanode and a metal counter electrode. As usual, the y-axis represent the energy of an electron at a certain point x in the cell. The energy of an electron in vacuum at infinite distance is chosen as a reference. It is important to note that the vacuum level bends in the presence of an

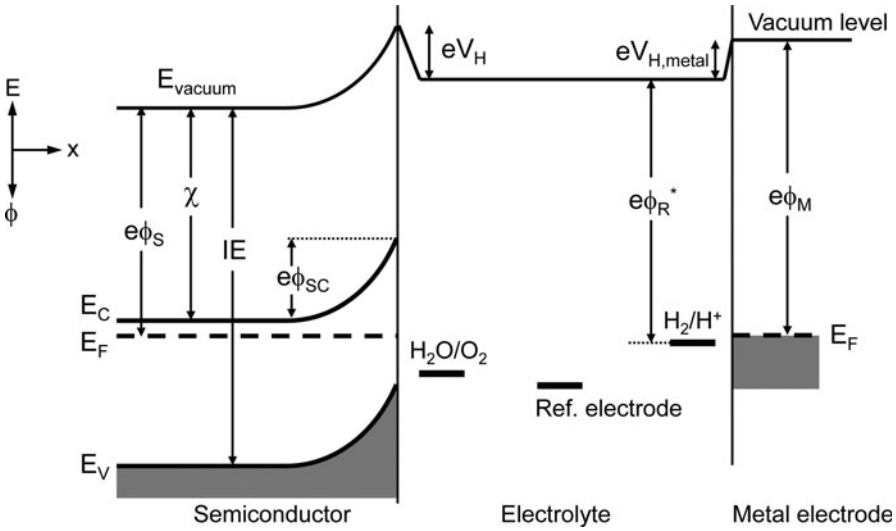

Fig. 2.16 Energy diagram for a PEC cell based on a n-type semiconductor and a metal counter electrode. The vacuum energy level is taken as a reference; this is the energy of an electron in vacuum at infinite distance. The electron affinity (χ) and ionization energy (IE) are materials constants, whereas the semiconductor work function (ϕ_S) also depends on the distance to the surface. Note that a Helmholtz layer is also present at the metal/electrolyte interface

electric field, i.e., it follows the potential gradients that are present in the PEC cell. This may seem a bit odd for a "reference" energy, but it is a consequence of the convention that the electrochemical potential (or Fermi energy) of the electrons is drawn as a constant value when the system is in equilibrium.

We now take a closer look at the electrolyte phase in Fig. 2.16. The energy of a redox couple in an electrolyte with respect to the vacuum level ($e\phi_R$*) is not accurately known. Theoretical and experimental estimates place the H_2/H^+ standard redox energy between 4.3 and 4.85 eV below E_{vacuum} [43]. Usually a value of 4.5 eV is taken, but it should be realized that this value has an uncertainty of a few tenths of an eV; Bockris suggested a value of (4.6 ± 0.2) eV [42]. The value recommended by IUPAC is (4.44 ± 0.02) eV [44]. The vacuum level has been drawn as a horizontal line in the electrolyte, since no electric field is assumed to be present in this phase. This is a realistic assumption for most water splitting applications because highly concentrated electrolytes are used in order to avoid Ohmic voltage losses. For very low electrolyte concentrations (<0.1 M), there may be insufficient ions available at the outer Helmholtz plane to compensate all the adsorbed charges at the semiconductor surface. These charges are then compensated in a region that extends much beyond the outer Helmholtz plane, the so-called *Gouy layer*. The potential distribution in this layer resembles that of a SCR in a semiconductor and is described by the Gouy–Chapman theory. Since the Gouy layer is rarely relevant for solar water splitting applications, we refer the reader to the literature for a more detailed description [42].

The key parameters for the semiconductor are the band positions, the amount of band bending, and the difference between E_C and E_F. The latter depends on the free electron concentration in the bulk ($= N_D^+ - N_A^-$) and can be calculated by (2.9). The energy diagram directly shows whether a certain reduction or oxidation reaction at the semiconductor surface is thermodynamically possible. In the example of Fig. 2.16, photogenerated holes will be able to oxidize water if the H_2O/O_2 redox energy is positioned above the top of the valence band. Similarly, only electrons with an energy above the redox energy can reduce the corresponding species in the electrolyte. By measuring the potential (i.e., the Fermi level) of the semiconductor with respect to that of a reference electrode, its reduction or oxidation power can be determined. The advantage of using a reference electrode for this is that the measured potential difference does not depend on the amount of current that flows through the cell. In contrast, the potential difference between the semiconductor and the metal counter electrode depends on V_H at the metal electrode (i.e., the overpotential), which depends on the current in an unknown way.

Because of the high concentration of free electrons in the metal counter electrode, the SCR inside the metal is extremely thin (~1 Å) and can therefore be ignored. The structure of the Helmholtz layer at the metal/electrolyte interface is similar to that described for the semiconductor, and the capacitance is also in the order of 10–20 μF/cm^2. As already hinted in the previous paragraph, the potential drop across the Helmholtz layer depends on the kinetics of electron transfer across the interface. This is because any overpotential applied to a metal electrode must fall across the Helmholtz layer. This is quite different from the case of an external potential applied to a semiconductor electrode, which is discussed in the next section.

2.6.4 Applying A Bias Potential

The operation of a PEC cell can be influenced by applying an external bias potential to the semiconductor. When the bias is applied with respect to a reference electrode, the potential difference will be distributed over the space charge layer and the Helmholtz layer. These layers act as two capacitances in series [41]:

$$\frac{1}{C_{tot}} = \frac{1}{C_{SC}} + \frac{1}{C_H}. \tag{2.50}$$

Both layers have the same charge Q associated with them (this is the charge that is located at the inner Helmholtz plane), and since $C = Q/V$ the potential distribution is given by

$$\frac{\Delta V_{SC}}{\Delta V_H} = \frac{C_H}{C_{SC}}. \tag{2.51}$$

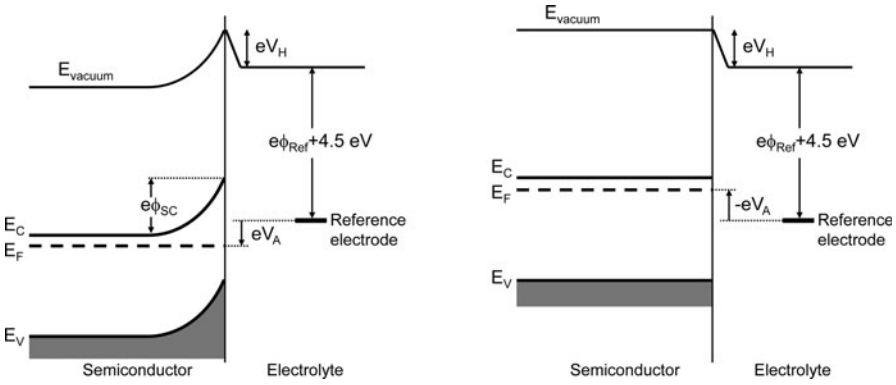

Fig. 2.17 Effect of applying a bias voltage (V_A) to an n-type semiconductor electrode. Any change in applied potential falls across the space charge layer, whereas V_H remains constant. In the picture on the left, a positive potential is applied to the semiconductor. When a sufficiently negative bias is applied, the band bending can be reduced to zero (*right*)

Because $C_H \gg C_{SC}$ (see above), any change in applied bias will fall across the depletion layer of the semiconductor.[9] This important conclusion is illustrated in Fig. 2.17. As shown in this figure, applying a positive bias to an n-type semiconductor results in an increase of the depletion layer. For a p-type semiconductor, a negative bias is required to increase the depletion layer. The ability to change the band bending in a semiconductor electrode is immensely useful in the characterization of these materials, as we see in later chapters.

2.6.5 pH Dependence of The Band Edges

While V_H is not affected by the applied bias potential, it does depend on the pH of the solution as described by (2.49). This means that the positions of the band edges shift with −59 mV per pH unit with respect to the redox potentials in the electrolyte. At first sight, this seems to be a very useful property: if reduction of a certain species is not possible because the conduction band is too low in energy, one might consider increasing the pH toward more alkaline values to make V_H more negative and raise E_C with respect to E_{redox} (a consequence is of course that this also increases E_V, so it reduces the oxidation power of the semiconductor). Unfortunately, this strategy does not help for water splitting because the reduction and oxidation potentials of water also depend on the pH via the Nernst equation. For reactions (2.1) and (2.2) in Sect. 2.2, the Nernst equations read:

[9] Note that in highly doped semiconductors ($>10^{19}$ cm^{-3}) and metals, C_{SC} can exceed C_H so that any change in the applied potential will fall across the Helmholtz layer instead of the depletion layer.

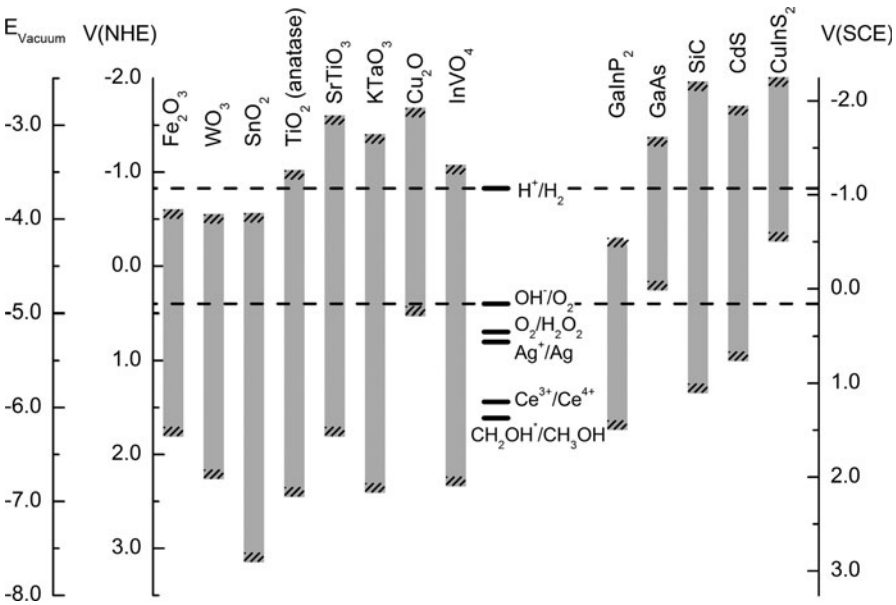

Fig. 2.18 Band edge positions for selected semiconductors at pH 14, together with some important redox potentials. It should be realized that the uncertainty in the band edge positions can amount to a few tenths of an eV for most semiconductors shown here

$$E_{\mathrm{red}} = E^0_{\mathrm{red}} - \frac{RT}{4F}\ln\left(\frac{p^2_{\mathrm{H_2}}}{[\mathrm{H^+}]^4}\right) = E^0_{\mathrm{red}} - \frac{2.3RT}{F}\left(\log\left(p^{1/2}_{\mathrm{H_2}}\right) + \mathrm{pH}\right) \tag{2.52}$$

$$E_{\mathrm{ox}} = E^0_{\mathrm{ox}} + \frac{RT}{4F}\ln\left(p_{\mathrm{O_2}}[\mathrm{H^+}]^4\right) = E^0_{\mathrm{ox}} + \frac{2.3RT}{F}(\log(p_{\mathrm{O_2}}) - \mathrm{pH}). \tag{2.53}$$

Hence, the reduction and oxidation potentials depend in the same way on the pH as the band positions, i.e., by −59 mV per pH unit. This means that the band positions of most metal oxides are fixed with respect to the water redox potentials.

Knowledge of the band edge positions at the surface is very useful, since they determine the maximum reduction and oxidation potentials of the photogenerated electrons and holes in a semiconductor. Figure 2.18 shows the band edge energies for several important semiconductors, together with the redox potentials for water splitting. The diagram is valid for a pH of 14. As outlined above, the band positions of most metal oxides show the same pH dependence as the water reduction and oxidation potentials, so relative positions remain the same at other pH values. This is, however, not the case for semiconductors and redox couples that do *not* show a -59 mV/pH dependence (MoS_2, Ce^{3+}/Ce^{4+}, Ag^+/Ag, etc.).

It should be noted that the actual reduction power of the electrons in a photoanode is always less than that suggested by the conduction band edge.

The same is true for the oxidative power of holes generated in a photocathode. This is because the photogenerated carriers lose some of their energy while traversing the SCR. Some more energy is lost when they leave the majority carrier band of the semiconductor and enter the metal counter electrode at its Fermi level. For an n-type semiconductor, the total energy loss is given by $E_{\text{loss}} = e\phi_{\text{SC}} + (E_{\text{C}} - E_F)$, and typically amounts to 0.1–0.5 eV.

2.6.6 The Flatband Potential

The position of the band edges with respect to the redox potentials in the electrolyte is conveniently expressed by the so-called "flatband potential", ϕ_{FB}. As the word suggests, this is the potential that needs to be applied to the semiconductor to reduce the band bending to zero. The flatband situation is illustrated in the right-hand panel of Fig. 2.17. It is important to realize that the flatband potential denotes the position of the *Fermi level* of the semiconductor with respect to the potential of the reference electrode. This means that ϕ_{FB} is slightly below the conduction band edges shown in Fig. 2.18, and that it *accurately reflects the thermodynamic ability of an n-type semiconductor to reduce water to hydrogen*.

Several techniques can be used to determine the flatband potential of a semiconductor. The most straightforward method is to measure the photocurrent onset potential, ϕ_{onset}. At potentials positive of ϕ_{FB} a depletion layer forms that enables the separation of photogenerated electrons and holes, so one would expect a photocurrent. However, the actual potential that needs to be applied before a photocurrent is observed is often several tenths of a volt more positive than ϕ_{FB}. This can be due to recombination in the space charge layer [45], hole trapping at surface defects [46], or hole accumulation at the surface due to poor charge transfer kinetics [43]. A more reliable method for determining ϕ_{FB} is electrolyte electroreflectance (EER), with which changes in the surface free electron concentration can be accurately detected [47]. The most often used method, however, is Mott–Schottky analysis. Here, the $1/C_{\text{SC}}{}^2$ is plotted as a function of the applied potential ϕ_{A}, and the value of the flatband potential is given by the intercept on the potential axis. This can be seen from a more commonly used version of equation, (2.42), in which ϕ_{SC} is replaced by $\phi_{\text{A}} - \phi_{\text{FB}}$:

$$\frac{1}{C_{\text{SC}}^2} = \frac{2}{\varepsilon_0 \varepsilon_{\text{r}} e N_{\text{D}} A^2} \left(\phi_{\text{A}} - \phi_{\text{FB}} - \frac{kT}{e} \right). \tag{2.54}$$

Any change of the potential across the Helmholtz layer is directly reflected in the flatband potential, so it is expected to shift by −59 mV per pH unit. This has indeed been experimentally observed for most metal oxides (e.g., TiO_2, ZnO, Fe_2O_3, SnO_2, WO_3) and even some nonoxide semiconductors (Ge, GaAs, $GaAs_{1-x}P$) [41, 48].

2.6.7 Surface and Interface States

Illumination of a semiconductor can lead to a change in the flatband potential, even at constant pH. This can be explained by the presence of surface states that trap photogenerated minority carriers [49]. The change in charge density at the interface (more specifically: the inner Helmholtz plane) results in a change in the Helmholtz potential and, therefore, the flatband potential. This is usually referred to as "unpinning of the band edges." The change in flatband potential can be used to determine the density of surface states involved:

$$\Delta Q_{SS} = C_H\left(\phi_{FB}^{light} - \phi_{FB}^{dark}\right). \tag{2.55}$$

The presence of surface states can also affect the band bending in the dark. If a high density of partially filled mono-energetic surface states is present, the Fermi level will be located somewhere halfway the surface state DOS. Any change in pH or applied potential will then be accommodated by a change in the occupation of this state and a concomitant change in the potential across the Helmholtz layer. If the surface state DOS is sufficiently high, the Fermi level will show only a very small shift, and the amount of band bending in the semiconductor remains constant. This is called "Fermi level pinning". It is fairly common in covalent semiconductors, where it can be recognized by a different amount of band bending upon forming a metal–semiconductor Schottky contact that would be expected from the work function difference between both phases. It can also be observed as a flat region in a Mott–Schottky plot because the capacitance of the depletion layer will remain constant, while the Fermi level crosses the surface state energy. The physical origin of surface or interface states can have structural defects (dangling bonds, vacancies, etc.) or chemisorbed species from an electrolyte solution. In metal oxide semiconductors, the surface state DOS is generally small and Fermi level pinning is rarely observed. However, it is important in tandem devices or photocatalysts based on a junction between covalent and metal oxide semiconductors, e.g., n-Si/n-TiO_2 [50].

The chemical nature of surface states depends strongly on the bonding character of the material. Covalent materials have dangling bonds that can act as electron donors or acceptors – these are called *Shockley surface states*. Moreover, overlap between neighboring bonds can result in the formation of coupled states that have bonding (donor) and antibonding (acceptor) character. In ionic materials, so-called *Tamm states* are formed by coordinatively unsaturated ions at the surface. For example, lattice oxygen at the surface (O_L^{z-}) generally forms a deep donor state just above the valence band, while lattice metal ions (M_L^{x+}) can form deep acceptor states just below the conduction band [41]. In addition to these intrinsic surface states, extrinsic surface states can be formed by the adsorption of ions from the solution.

2.6.8 *Interfacial Electron Transfer*

In the discussion so far, electron transfer from the semiconductor to the electrolyte is assumed to be possible if the energy of the electron in the solid exceeds the reduction energy of the species in the solution (and vice versa). Unfortunately, this simple picture does not hold for large energy differences. Moreover, it does not give any information on the kinetics of electron transfer. A more detailed theory of electron transfer was developed in the late 1950s by Marcus [51, 52], who won the 1992 Nobel Prize in Chemistry for his contributions in this field. His theory is mainly based on classical physics, and is applicable to both homogeneous systems and reactions at electrodes. Quantum-chemical extensions of the theory were later made by the Russian scientists Levich, Dogonadze, and Kuznetsov [43]. The most useful contribution to electrochemistry was made in the early 1960s by Gerischer [53]. Whereas Marcus derived his theory using configurational coordinate diagrams of the Gibbs free energy of the species involved, Gerischer approached the problem using electronic energy levels. We follow his approach in the description below.

A common element in all versions of electron transfer theory is the concept of fluctuating energy levels in the electrolyte. In polar solvents, such as water, every ion in the electrolyte is surrounded by a cloud of oriented solvent molecules (cf. Fig. 2.15). In addition to these nearest-neighbor solvent molecules in the so-called *inner sphere*, the ion also has Coulomb interactions with polar solvent molecules and other ions that are farther away in the *outer sphere*. Due to the thermal motions of the solution, the energy level of the central ion (as seen from the electrode) will fluctuate. Moreover, after reduction or oxidation of the ion, the surrounding solvent molecules and ions will rearrange themselves to accommodate the different charge on the ion. The electrostatic energy required for this reorganization is given by 2λ, where λ is called the *reorganization energy*. It can be shown that the chance for a reduced or oxidized species to have a certain energy E is given by [53]:

$$W_{\mathrm{ox}}(E) = \frac{1}{\sqrt{4\pi\lambda kT}} \mathrm{Exp}\left(\frac{-\left(E - E^0_{\mathrm{redox}} + \lambda\right)^2}{4kT\lambda}\right) \tag{2.56}$$

$$W_{\mathrm{red}}(E) = \frac{1}{\sqrt{4\pi\lambda kT}} \mathrm{Exp}\left(\frac{-\left(E - E^0_{\mathrm{redox}} - \lambda\right)^2}{4kT\lambda}\right). \tag{2.57}$$

Here, E^0_{redox} is the standard redox potential for the species involved. The distribution of these fluctuating energy levels is shown in Fig. 2.19. It should be emphasized that this is a *probability distribution* – it should not be confused with the DOS, which is a fundamentally different concept (only one level exists at any one time for every ion, so optical transitions between the redox levels are not possible). The reorganization energy can be quite large compared to the bandgap of the semiconductor,

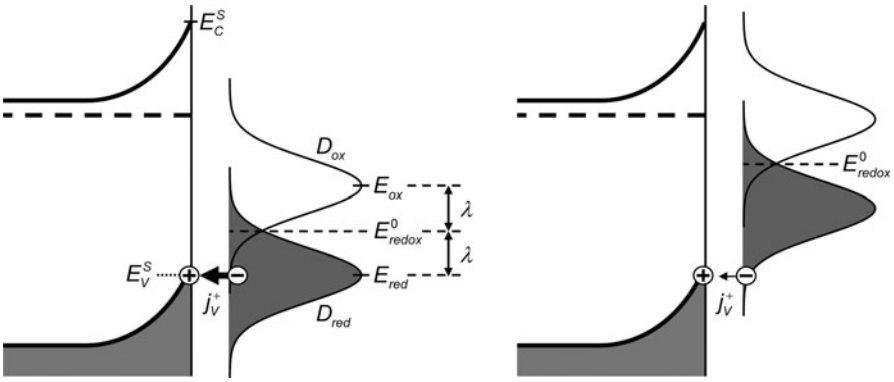

Fig. 2.19 Energy level model for electron transfer from a redox species in the electrolyte to a photogenerated hole in the semiconductor valence band. The density of states D_{red} depend on the concentration of the reductant species according to $D_{\mathrm{red}} = c_{\mathrm{red}} W_{\mathrm{red}}(E)$. A large overlap of the redox DOS with the energy of the hole (*left*) gives higher currents than a small overlap (*right*)

with values ranging from 0.3 eV to more than 1 eV. At room temperature, the width of each distribution curve (at half height) is given by $\Delta E \simeq 0.53\sqrt{\lambda}$ (in eV).

For semiconductors, charge transfer takes place via either the bottom of the conduction band or the top of the valence band. In certain cases, charge transfer via surface states can also occur. Although Fig. 2.19 is drawn for the case of electron transfer to the valence band, which will only be significant if photogenerated holes are present, similar pictures can be made for other pathways, e.g., $D_{\mathrm{red}} \rightarrow E_{\mathrm{C}}$, $E_{\mathrm{C}} \rightarrow D_{\mathrm{ox}}$, or $E_{\mathrm{V}} \rightarrow D_{\mathrm{ox}}$. An important conclusion from Fig. 2.19 is that the probability of electron transfer actually *decreases* if E_{red} is too far above E_{V}^S. This is markedly different from the behavior of metal electrodes, which show a continuous increase in current with applied potential.

The actual charge transfer process takes place via tunneling. Since tunneling is an iso-energetic process, it requires the fluctuating energy level of the species in the electrolyte to be, at a certain moment in time, equal to the energy of the electron or hole in the semiconductor. During electron transfer, the energy level of the ion is assumed to remain constant. This assumption (the so-called *Frank–Condon principle*) is justified, since electron transfer processes occur on a much faster time scale than ionic reorganization. The transfer rate is then proportional to the concentration of the relevant carrier in the semiconductor, the DOS of the electrolyte species ($D_{\mathrm{ox,red}} = c_{\mathrm{ox,red}} W_{\mathrm{ox,red}}(E)$), and a quantum-mechanical tunneling coefficient. With this approach, the anodic (+) and cathodic (−) valence and conduction band currents can then be written as [53]:

$$j_{\mathrm{V}}^{+} = e k_{\nu}^{+} p_{\mathrm{S}} c_{\mathrm{red}} W_{\mathrm{red}}(E_{\mathrm{V}}^S) \quad j_{\mathrm{V}}^{-} = e k_{\nu}^{-} N_{\mathrm{V}} c_{\mathrm{ox}} W_{\mathrm{ox}}(E_{\mathrm{V}}^S) \tag{2.58}$$

$$j_{\mathrm{C}}^{+} = e k_{\mathrm{c}}^{+} N_{\mathrm{C}} c_{\mathrm{red}} W_{\mathrm{red}}(E_{\mathrm{C}}^S) \quad j_{\mathrm{C}}^{-} = e k_{\mathrm{c}}^{-} n_{\mathrm{S}} c_{\mathrm{ox}} W_{\mathrm{ox}}(E_{\mathrm{C}}^S). \tag{2.59}$$

Here, N_C and N_V are the effective density of states in the semiconductor, and n_S and p_S are the surface concentrations of free electrons and holes in the conduction and valence bands, respectively. Further analysis leads to the following expressions for the overall conduction and valence band currents as a function of the overpotential η in the presence of a redox species:

$$j_V = j_V^0\left(\exp\left(\frac{-e\eta}{kT}\right) - 1\right) \quad \text{and} \quad j_C = -j_C^0\left(\exp\left(\frac{-e\eta}{kT}\right) - 1\right). \tag{2.60}$$

It is instructive to compare this with the Butler–Volmer equation for the current at a *metal* electrode:

$$j = j_0\left(\exp\left(\frac{(1-\alpha)e\eta}{kT}\right) - \exp\left(\frac{-\alpha e\eta}{kT}\right)\right). \tag{2.61}$$

Here, α is the so-called transfer coefficient, which is ~0.5 for metal electrodes. A Tafel plot of $\log(j/j_0)$ vs. η gives a slope of ~60 mV per current decade for a semiconductor, whereas a slope of ~120 mV/decade is found for a metal. The difference is caused by the fact that the applied overpotential falls across the Helmholtz layer for a metal, and across the SCR for a semiconductor. An even more crucial difference is not immediately apparent from (2.60) and (2.61): the exchange current density for a semiconductor is much smaller than that for a metal. This is a direct consequence of the high density of states of a metal near its Fermi level, which can be 3–4 orders of magnitude higher than N_C and N_V in a semiconductor. In fact, the current flowing at a semiconductor photoelectrode in the dark is usually negligible (often <10 nA/cm^2). This dark current is mainly carried by the *majority* carriers, i.e., electrons in the conduction band for an n-type semiconductor, and holes in the valence band for a p-type material. Under illumination, the current increases and is dominated by the transfer of *minority* carriers across the semiconductor/electrolyte interface. This is discussed in the next section.

2.7 The Photoelectrochemical Cell Under Operating Conditions

Most of the discussions above concern the properties of the semiconductor and semiconductor/electrolyte interface under equilibrium conditions, i.e., in the dark. We now explore how the system behaves under illumination.

2.7.1 The Quasi-Fermi Level

Figure 2.20 shows the energy diagram of a PEC cell in the dark and under illumination. In this example, the H_2O/O_2 redox couple is assumed to be the most

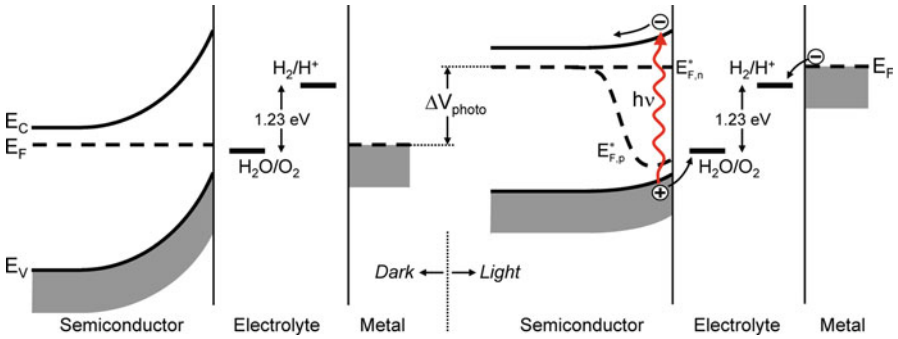

Fig. 2.20 Band diagram for a PEC cell based on an n-type semiconducting photoanode that is electrically connected to a metal counter electrode; in equilibrium in the dark (*left*) and under illumination (*right*). Illumination raises the Fermi level and decreases the band bending. Near the semiconductor/electrolyte interface, the Fermi level splits into quasi-Fermi levels for the electrons and holes

active species and therefore dominates the electrochemical potential of the solution in the dark. The Fermi levels of the semiconductor and metal, which are electrically connected, adjust to a value close to E_{ox}. Upon illumination, electron–hole pairs are created and the Fermi level increases with ΔV_{photo}, the internal photovoltage. Since the system is no longer in equilibrium, particularly in the SCR where the electrons and holes are generated, the use of a single Fermi level is no longer appropriate. Instead, the concept of *quasi-Fermi levels* is more useful. The quasi-Fermi levels are a direct measure of the concentration of electrons and holes at a certain point x in the semiconductor, and are defined as:

$$n = n_0 + \Delta n = N_C \, e^{-\left(E_C - E^*_{F,n}\right)/kT} \tag{2.62}$$

$$p = p_0 + \Delta p = N_V \, e^{-\left(E^*_{F,p} - E_V\right)/kT}. \tag{2.63}$$

Here, n_0 and p_0 are the equilibrium carrier concentrations in the dark, and Δn and Δp are the additional carriers created by illumination. For an n-type semiconductor, $n = n_0 + \Delta n \approx n_0$ and $p = p_0 + \Delta p \approx \Delta p$ so that $E^*_{F,n}$ remains horizontal whereas $E^*_{F,p}$ departs from the bulk Fermi level in the active region.

The quasi-Fermi level is often interpreted as a thermodynamic driving force. Whether or not this is appropriate is a matter of some debate. While it may provide useful insights, the concept has been derived from kinetic arguments, and can at best provide a quasi-thermodynamic description. Whereas true equilibrium thermodynamics are universally valid, the predictive value of the quasi-Fermi level as a thermodynamic driving force for, e.g., chemical reactions may depend on the reaction mechanism. One particular aspect to be noted in this respect is that the quasi-Fermi level definitions in (2.62) and (2.63) only consider electrons and holes in the conduction and valence bands. They do not account for any changes in the

occupation of surface or bulk defect states, which limits their predictive value for reactions in which these states are involved.

2.7.2 Photocurrent–Voltage Characteristics

The theoretical description of semiconductor photocurrent–voltage characteristics have received considerable attention in the literature. One of the most often used models was reported by Gärtner [45], who derived the following expression for the photocurrent in a semiconductor under reverse bias:

$$j_G = j_0 + e\Phi\left(1 - \frac{\mathrm{Exp}(-\alpha W)}{1 + \alpha L_\mathrm{p}}\right). \tag{2.64}$$

Here, Φ is the incident light flux, α is the absorption coefficient (assuming monochromatic illumination), W is the depletion layer width, L_p is the hole diffusion length, and j_0 is the saturation current density. The model assumes that there is no recombination in the SCR and at the interface.

Gärtner's model was improved by Reichman [45], who used more appropriate boundary conditions for his derivation of the total valence band photocurrent in an n-type semiconductor:

$$j_\mathrm{V} = \frac{j_\mathrm{G} - j_0\,\mathrm{Exp}\left(\frac{-e\eta}{kT}\right)}{1 + \frac{j_0}{j_\mathrm{V}^0}\,\mathrm{Exp}\left(\frac{-e\eta}{kT}\right)}. \tag{2.65}$$

Here, j_V^0 is the hole transfer rate at the interface, and j_0 is the saturation current density, i.e., the hole current in the valence band at $x = W$ when $\Phi = 0$. η is the overpotential, which is defined as the difference between the applied potential and the open-circuit potential under illumination. Reichman's model includes the possibility of recombination in the SCR, which he showed could become important when the photovoltage becomes large enough for the bands to flatten. Another useful aspect of (2.65) is that it can be used to model the effect of the slow hole transfer kinetics that are often observed for metal oxides such as α-Fe_2O_3 [54]. The value of the saturation current density, $j_0 = (eL_\mathrm{p}N_\mathrm{C}N_\mathrm{V}/\tau N_\mathrm{D})\mathrm{Exp}\,(-E_\mathrm{g}/kT)$, plays an important role in Reichman's model, especially for narrow-bandgap semiconductors with large hole diffusion lengths and low donor densities. If the bandgap exceeds ~1.8 eV, which is the case for almost all metal oxides, j_0 becomes negligible and (2.64) and (2.65) give almost indistinguishable results.

At about the same time as Reichman, Jarrett also published a model that explicitly included recombination in the SCR [55]. For a given impurity concentration, the numerical solutions for the photoconversion efficiency he obtained are completely defined by three parameters: the optical absorption coefficient, the minority carrier lifetime in the depletion layer, τ_R, and the charge transfer rate at

the surface. In Jarrett's model the amount of recombination in the space charge is expressed as (τ_t/τ_R), where τ_t is the time needed for the minority carriers to traverse the SCR. The usefulness of this approach is demonstrated in Chap. 9, where Jarrett's model is used to establish design criteria for photoelectrodes based on low-mobility (i.e., small polaron) semiconducting metal oxides.

It should be emphasized that the previous models only describe the current due to *minority carriers*. Under near-flatband conditions, the majority carriers start to contribute to the overall current. This can be recognized by an increase in the dark current, and under those conditions (2.64) and (2.65) are no longer useful. Another implicit assumption is the absence of mass transport limitations in the electrolyte, but this is rarely an issue in photoelectrochemistry due to the high electrolyte concentrations and modest efficiencies reported thus far. Finally, it should be realized that the models described above cannot account for recombination at the semiconductor/electrolyte interface. Wilson published an extension of Gärtner's original model that included interfacial recombination effects [56]. Although this somewhat complicated model is not often used because it does not account for the dark current and recombination in the space charge, it is of value for metal oxides that show extensive surface recombination.

2.7.3 Reaction Mechanisms

One of the main bottlenecks for water splitting is the oxidation half-reaction, which is a complicated process involving four separate electron transfer steps. Little is known about the exact molecular reaction mechanism of water oxidation on metal oxide surfaces. The only exception is TiO_2, which has been extensively investigated. Early work suggested that surface Ti–OH^- groups are photo-oxidized to Ti-$OH^{\bullet}$ radicals, which further react to adsorbed H_2O_2 species and finally to O_2 [57]. Nakato et al. proposed an alternative mechanism based on a nucleophilic attack of a H_2O molecule on a surface-trapped hole on a lattice oxygen site. The proposed reaction mechanism is shown in Fig. 2.21 [58, 59]. This mechanism served as a basis for recent theoretical DFT studies on the water oxidation reaction at various metal oxide surfaces [60–62]. For TiO_2, the reaction of water molecules with surface vacancies to form adsorbed hydroxyl groups was proposed to be the rate-determining step [61]. In contrast, the rate-limiting step for WO_3 appears to be the transfer of a proton from the surface adsorbed hydroxyl group to the electrolyte [62]. Although there remains some uncertainty about the actual molecular reaction mechanisms, these theoretical studies can provide valuable pointers for rational photoanode design [60].

Since the overpotential for water oxidation can easily exceed 0.6 V for a metal oxide photoanode, co-catalysts are often used to enhance the reaction kinetics. IrO_2 and RuO_2 are well-known oxidation catalysts, but they are either prohibitively expensive or prone to photocorrosion [63]. Recently, low-cost and stable

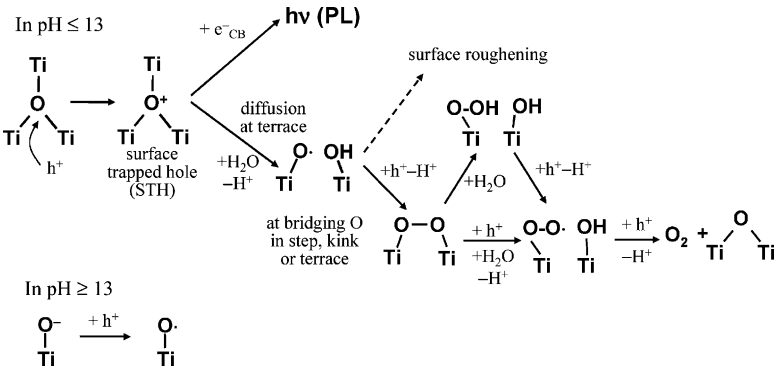

Fig. 2.21 Reaction mechanism for water oxidation on a rutile TiO_2 surface proposed by Nakato et al. Reprinted with permission from [59]. Copyright 2007 American Chemical Society

alternatives based on, e.g., cobalt have been found [64, 65]. Such catalysts have indeed been reported to enhance the efficiency of hematite photoanodes [66].

The reduction of water is a much simpler two-electron process. Many n-type semiconductors can evolve hydrogen at small overpotentials and without a co-catalyst. In contrast, p-type photoelectrodes generally require a large overpotential for the onset of cathodic photocurrents, and noble metal co-catalysts are often required [43]. Few p-type semiconductors have a conduction band that is well above the hydrogen reduction energy. Notable exceptions are SiC [67] and Cu_2O [68]. An important advantage of p-type photoelectrodes is that anodic decomposition, which is often observed for n-type photoelectrodes, does not occur. Having said this, it should be noted that the stability of many p-type oxides (Cu_2O, delafossites) in aqueous environments is notoriously poor.

2.7.4 Photocorrosion

Photocorrosion occurs when the photogenerated holes do not oxidize water, but the semiconductor itself. The general form of this anodic decomposition reaction can be written as

$$M_xO_y + \frac{2y}{x}h^+ \underset{}{\overset{\text{electrolyte}}{\rightleftharpoons}} xM_{(aq)}^{(2y/x)+} + \frac{y}{2}O_2. \tag{2.66}$$

A well-known oxide that suffers from severe photocorrosion in aqueous environments is ZnO. For p-type oxides, cathodic photoreduction can lead to the formation of metal deposits:

$$M_xO_y + 2ye^- + 2yH_{(aq)}^+ \overset{\text{electrolyte}}{\rightleftharpoons} xM_{(s)} + yH_2O. \tag{2.67}$$

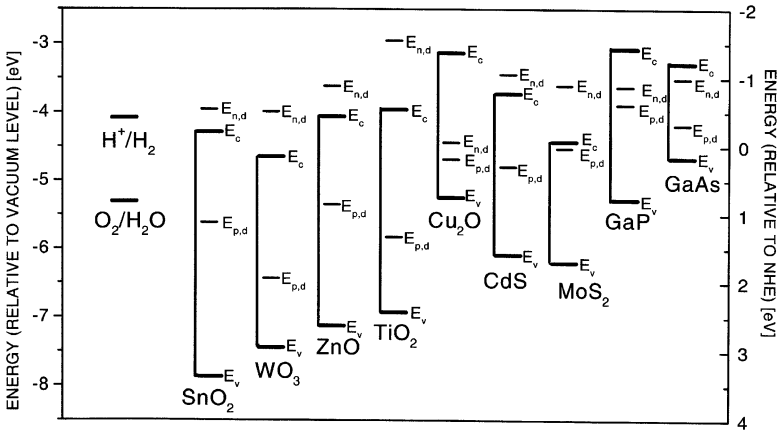

Fig. 2.22 Position of decomposition potentials of selected semiconductors. Reprinted from [70], with permission from Elsevier

In an alkaline environment, the reaction can be written as

$$M_xO_y + 2ye^- + yH_2O \underset{\rightleftharpoons}{\overset{\text{electrolyte}}{\rightleftharpoons}} xM_{(s)} + 2yOH^-_{(aq)}. \tag{2.68}$$

This has been observed for, e.g., Cu_2O. Alternatively, protons can enter the metal oxide lattice when free electrons are available at or near the surface, a process known as *intercalation*. It is worth mentioning that III–V semiconductors, such as GaAs and GaP, are prone to anodic photocorrosion, but appear to be relatively stable against cathodic photocorrosion in practice [69].

Whether or not these highly undesired reactions occur depends on their equilibrium potentials, which are in turn related to the Gibbs free energy of the reactions, cf. (2.5). If the energy level for anodic decomposition, $E_{p,decomp}$, is below the valence band maximum, no anodic decomposition can occur. Conversely, if $E_{n,decomp}$ is above the conduction band minimum, no cathodic photocorrosion can occur [41]. An overview of the anodic and cathodic decomposition potentials for various semiconductors is shown in Fig. 2.22. The actual values of the decomposition potentials depends on the concentration of the reaction products via the Nernst equation, so that they may depend on the pH of the solution [71]. A somewhat dated but useful overview of the stability of various metal oxides against photoanodic decomposition as a function of pH has been given by Scaife [72]. While some metal oxides are thermodynamically stable against cathodic photocorrosion (e.g., TiO_2), most – if not all – known metal oxides are thermodynamically unstable against anodic photocorrosion. This is also evident from the positions of $E_{p,decomp}$ in Fig. 2.22. This is even the case for n-type photoanodes that are found to be very stable, such as TiO_2 and α-Fe_2O_3; decomposition of these materials is simply inhibited by slow reaction kinetics. If a material shows signs of photocorrosion,

the addition of suitable co-catalysts may alleviate the problem to some extent by favoring the water oxidation route. In practice, photocorrosion is difficult to predict and one usually has to put new materials to the test under actual operating conditions.

2.8 Energy and Quantum Conversion Efficiencies

The energy conversion efficiency is one of the key performance indicators of the PEC cell. Assuming that all the photogenerated electrons and holes are used for the water splitting reaction, the overall solar-to-hydrogen efficiency is given by

$$\eta_{\mathrm{STH}} = \frac{P^{\mathrm{out}}_{\mathrm{electrical}} - P^{\mathrm{in}}_{\mathrm{electrical}}}{P_{\mathrm{light}}} = \frac{j_{\mathrm{photo}}(V_{\mathrm{redox}} - V_{\mathrm{bias}})}{P_{\mathrm{light}}}. \tag{2.69}$$

V_{redox} is usually taken to be 1.23 V (at room temperature), based on a Gibbs free energy change for water splitting of 237 kJ/mol. Alternatively, the enthalpy change (286 kJ/mol) is sometimes used, which corresponds to a redox potential of 1.48 V. The latter value is appropriate when the hydrogen produced will be used in a combustion process, whereas the former value is more appropriate when the hydrogen is converted into electricity in a fuel cell [69]. When the end-use of the produced H_2 is not clear, it is probably best to use the Gibbs free energy value since it yields more conservative efficiency numbers. Assuming AM1.5G incident sunlight ($P_{\mathrm{light}} = 1{,}000$ W/m^2) and no applied bias, the efficiency can be directly related to the photocurrent by $\eta_{\mathrm{STH}} = 1.23 \times j_{\mathrm{photo}}$, with the efficiency in % and the photocurrent in mA/cm^2. Hence, a photocurrent of ~8 mA/cm^2 is required to reach the 10% efficiency target for economically viable PEC cells (see Chap. 8).

It should be emphasized that V_{bias} in (2.69) refers to the actual potential difference between the working and counter electrodes. Attempts to indirectly determine this potential difference from the results of a three-electrode measurement (in which the working electrode potential is reported relative to that of a reference electrode) generally leads to errors, and should be avoided (see also Chap. 3).

A more direct method to determine the solar-to-hydrogen efficiency is to measure the amount of evolved hydrogen by mass spectrometry, gas chromatography [73, 74], or by following the water displacement in an inverted burette. The STH efficiency for this approach is given by

$$\eta_{\mathrm{STH}} = \frac{\Phi_{\mathrm{H_2}} G^0_{\mathrm{f,H_2}}}{P_{\mathrm{light}}}, \tag{2.70}$$

where $\Phi_{\mathrm{H_2}}$ is rate of H_2 evolution at the illuminated area (mol/s/m^2) and $G^0_{\mathrm{f,H_2}}$ is the Gibbs free energy of formation of hydrogen (237 kJ/mol).

When reporting STH efficiencies, care should be taken to ensure that (a) the water splitting reaction is stoichiometric (H_2:O_2 = 2:1), (b) no other reactions due to, e.g., sacrificial donors/acceptors occur, and (c) the light source is well specified and closely matches the AM1.5G spectrum in intensity and spectral distribution [75]. For more detailed information on STH efficiency measurements, the reader is referred to some useful guidelines reported by a US Department of Energy (DOE) working group on photoelectrochemical hydrogen production [76] and to a careful study on the influence of the type of light source used [77].

When trying to identify performance-limiting factors in PEC photoelectrodes, the quantum efficiency as a function of wavelength is a particularly useful parameter. The definition of the *external* quantum efficiency is the fraction of the incident photons that is converted to electrons that can be measured by the outer circuit. This is the IPCE (*incident photon-to-current conversion efficiency*), which is given by

$$\mathrm{IPCE}(\lambda) = \frac{hc}{e}\left(\frac{j_{\mathrm{photo}}(\lambda)}{\lambda P(\lambda)}\right). \tag{2.71}$$

IPCE values in excess of 80% for the photo-oxidation of water have been reported for, e.g., WO_3 [78] and for TiO_2 under UV illumination [79]. Another useful parameter is the APCE, or *absorbed photon-to-current conversion efficiency*. In contrast to the IPCE, the APCE also corrects for reflection losses. Often referred to as the *internal* quantum efficiency, it is related to the IPCE via

$$\mathrm{APCE}(\lambda) = \frac{\mathrm{IPCE}(\lambda)}{A(\lambda)} = \frac{\mathrm{IPCE}(\lambda)}{1 - R - T} \tag{2.72}$$

A, R, and T are the optical absorption, reflection, and transmission, respectively. The optical absorption is not to be confused with the *absorbance* or *optical density*, which is given by

$$\mathrm{OD} = -\mathrm{Log}\left(\frac{T}{1 - R}\right) = \frac{\alpha L}{2.303}. \tag{2.73}$$

Here, α is the absorption coefficient and L is the film thickness. The APCE is the more useful parameter when evaluating recombination within the semiconductor, while the IPCE is more appropriate to evaluate device-level conversion efficiencies.

Of particular interest is the use of IPCE values measured under monochromatic irradiation to predict the photocurrent under actual solar irradiation:

$$J_{\mathrm{solar}} = \int (\mathrm{IPCE}(\lambda) \times \Phi(\lambda) \times e)\, \mathrm{d}\lambda. \tag{2.74}$$

Here, J_{solar} is the total solar photocurrent in A/m^2 and $\Phi(\lambda)$ is the photon flux of sunlight in photons/m^2/s. The photon flux can be calculated from tabulated solar

irradiance data, $E(\lambda)$, via $\Phi(\lambda) = E(\lambda)/(hc/\lambda)$ [75]. An important underlying assumption for (2.74) is that there is a linear relationship between the monochromatic photocurrent and the light intensity. This is often the case, but there are exceptions. A super-linear increase of the photocurrent with light intensity is sometimes observed for nanostructured materials with high concentrations of relatively shallow surface or interface traps; these traps first need to be filled before the charge carriers can reach the electrolyte or the back contact [80]. Conversely, slow charge transport or charge transfer across the interface may lead to an accumulation of free charge carriers at or near the interface. This increases the amount of recombination and will result in a sublinear increase of the photocurrent with light intensity.

2.9 Photoelectrode Requirements and Cell Configurations

The most critical aspect of the design of a photoelectrochemical device for water splitting is the choice of suitable photoanode and/or photocathode materials. Several of the requirements imposed on these materials appear to be in conflict, and certain trade-offs have to be made. In some cases, these trade-offs can be avoided by adopting smart architectures and materials combinations. The remainder of this chapter gives a few general considerations and approaches; more detailed accounts of strategies to cope with these trade-offs are given in later chapters.

2.9.1 Requirements and Trade-offs

Most of the requirements for suitable water-splitting photoanode and/or photocathode materials have already been alluded to in the previous sections of this chapter. They can be summarized as follows [81]:

- Good (visible) light absorption
- High chemical stability in the dark and under illumination
- Band edge positions that straddle the water reduction and oxidation potentials
- Efficient charge transport in the semiconductor
- Low overpotentials for reduction/oxidation of water
- Low cost

The spectral region in which the semiconductor absorbs light is determined by the bandgap of the material. The minimum bandgap is determined by the energy required to split water (1.23 eV) plus the thermodynamic losses (0.3–0.4 eV [82]) and the overpotentials that are required at various points in the system to ensure sufficiently fast reaction kinetics (0.4–0.6 eV) [77, 83]. As a result, the bandgap should be at least 1.9 eV, which corresponds to an absorption onset at 650 nm. Below 400 nm the intensity of sunlight drops rapidly, imposing an upper limit of

3.1 eV on the bandgap. Hence, the optimum value of the bandgap should be somewhere between 1.9 and 3.1 eV, which is within the visible range of the solar spectrum. In a thorough analysis, Murphy et al. suggested an optimum bandgap of 2.03 eV, which would lead to a solar-to-hydrogen efficiency of 16.8% [77].

The chemical stability requirement is a severe one that limits the usefulness of many photo-active materials. Most nonoxide semiconductors either dissolve or form a thin oxide layer that prevents charge transfer across the semiconductor/electrolyte interface. Oxide semiconductors are more stable, but may be prone to anodic or cathodic decomposition, as outlined in Sect. 2.7.4. The general trend is that the stability against (photo)corrosion increases with increasing bandgap. Although this conflicts with the requirement of visible light absorption, a small bandgap and good chemical stability are not necessarily mutually exclusive (although one could argue that a small bandgap is often accompanied by a high valence band energy, which would indeed result in a less stable material).

Few semiconductors fulfill the third requirement, which states that the band edges should straddle the water reduction and oxidation potentials. As shown in Fig. 2.18, the ones that do either have a bandgap that is too large (e.g., $SrTiO_3$, SiC) or are unstable in aqueous solutions (Cu_2O, CdS). This figure also suggests that the band edges of nonoxide semiconductors tend to be better suited toward the reduction of water (high E_C), whereas those of oxide semiconductors favor water oxidation (low E_V). It should be mentioned that the third requirement is actually a bit more stringent than Fig. 2.18 suggests. As pointed out originally by Gerischer [84], and reiterated later by Weber [85], it is the *quasi-Fermi levels* that should straddle the water redox potentials. Although the interpretation of the quasi-Fermi level as a thermodynamic driving force may not be entirely appropriate under all conditions (cf. Sect. 2.7.1), using it within the context of the third requirement seems reasonable.

The fourth requirement, that of efficient charge transport, is easily fulfilled in some materials (TiO_2, WO_3), while in others it is one of the main causes of poor overall conversion efficiencies. A particularly important example of the latter is that of α-Fe_2O_3, which will be discussed in detail in Chap. 4. One can distinguish intrinsic and extrinsic charge transport factors. As outlined in Sect. 2.2, the electronic band structure of the material gives important clues with regard to the intrinsic charge carrier mobilities. Extensive overlap of metal 3d orbitals usually leads to high electron mobilities, whereas the overlap of O-2p orbitals determines the hole mobility in most metal oxides. Extrinsic factors, in particular shallow donors/acceptors and recombination centers, are perhaps even more important. For example, electron transport was found to be rate limiting in spray-deposited, undoped films of α-Fe_2O_3, whereas hole transport was found to be rate limiting after donor doping the material with silicon [86]. The susceptibility to recombination is often expressed as the carrier lifetime, τ_R, or the minority carrier diffusion length, L_D. They are related through

$$L_D \simeq \sqrt{D\tau_R}. \tag{2.75}$$

The diffusivity of the free carriers, D, is related to their mobility, μ, via the Nernst–Einstein equation:

$$D = \frac{kT\mu}{e}. \tag{2.76}$$

Values of L_D range from several nanometers in some oxides to several hundred micrometers in high-purity silicon.

For n-type semiconductors, the fifth requirement implies that hole transfer across the semiconductor/electrolyte interface should be sufficiently fast in order to compete with the anodic decomposition reaction. More generally, interfacial charge transfer should be fast enough to avoid the accumulation carriers at the surface, as this would lead to a decrease of the electric field and a concomitant increase in electron–hole recombination. To improve the kinetics of charge transfer, catalytically active surface species can be added. Examples of effective oxygen evolution catalysts are RuO_2 [87], IrO_x [88], and Co-based compounds [64], whereas Pt, Rh [89], Cr–Rh, RuO_2, or NiO_x [73, 90] are usually employed as a catalysts for hydrogen evolution.

At this time, no single material has been found that meets all these requirements. Four main trade-offs can be identified:

- Bandgap ↔ stability
- Photon collection ↔ charge transport
- Recombination ↔ catalysis
- Performance ↔ cost

The bandgap vs. stability issue has been discussed above. The second trade-off is especially important for semiconductors with a small absorption coefficient, such as metal oxides with an indirect bandgap. In these materials most of the electron–hole pairs are generated far away from the surface, and the carriers recombine before reaching the interface (cf. Fig. 2.23). The third trade-off reflects the tendency of catalytically active surface sites to also act as efficient recombination centers for electronic charge carriers. Moreover, certain co-catalysts for hydrogen or oxygen evolution may also enhance the back-reaction between H_2 and O_2. A well-known example is Pt. This may be a problem for cell designs in which the cross-over of gases generated at the (photo)anode and (photo)cathode cannot be avoided. Interestingly, NiO is an efficient hydrogen evolution catalyst at which the $H_2 + O_2$ back-reaction does not seem to occur [73]. The final trade-off reflects the main reason for the interest in low-cost metal oxides, since the economic viability of state-of-the-art multijunction devices based on, e.g., high quality III–V materials grown by MOCVD or MBE is doubtful [91].

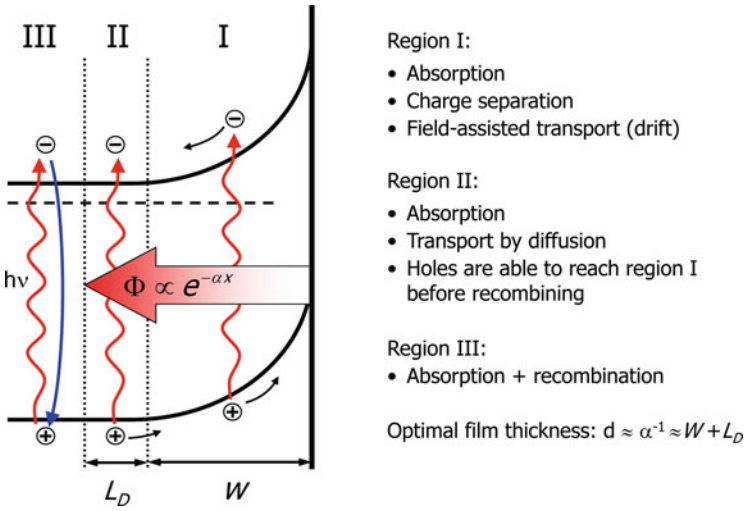

Fig. 2.23 Absorption regions in a semiconducting photoanode. The intensity of the light (Φ) decreases exponentially with distance from the surface (Lambert-Beer law). All charge carriers generated within a distance $L_D + W$ from the surface contribute to the photocurrent (regions I and II), whereas all carriers generated in region III recombine

2.9.2 Nanostructured Electrodes

Nanostructured electrode morphologies can be used to address some of the intrinsic material's limitations and trade-offs mentioned above. The most obvious advantage of a nanostructured morphology is the increase in specific surface area. The concomitant increase in the number of surface sites greatly enhances the overall charge transfer kinetics at the semiconductor/electrolyte interface.

A second advantage is the shorter diffusion path lengths for the photogenerated charge carriers. This is illustrated by the nanowire array photoelectrode shown in Fig. 2.24 (left), where the minority carriers only have to travel half the diameter of the nanowire in order to reach the semiconductor/electrolyte interface [92]. If transport of majority carriers is also an issue, one could employ an array of a conducting wires, which are coated with a thin film of the photoactive semiconductor (Fig. 2.24, right). Here, both minority and majority carriers benefit from the short distance ($\leq d$) that they have to travel before reaching the electrolyte and conducting core, respectively. This is sometimes referred to as a "guest–host" structure, in which the light absorbing nanosized guest material is attached to a nanostructured host scaffold [93]. The advantages are not limited to the highly regular nanowire array architecture shown in Fig. 2.24; nanostructures based on dendritic or cauliflower-type morphologies or randomly packed spheres offer similar advantages [78, 93, 94]. Such structures are discussed in more detail in Chaps. 4 and 9.

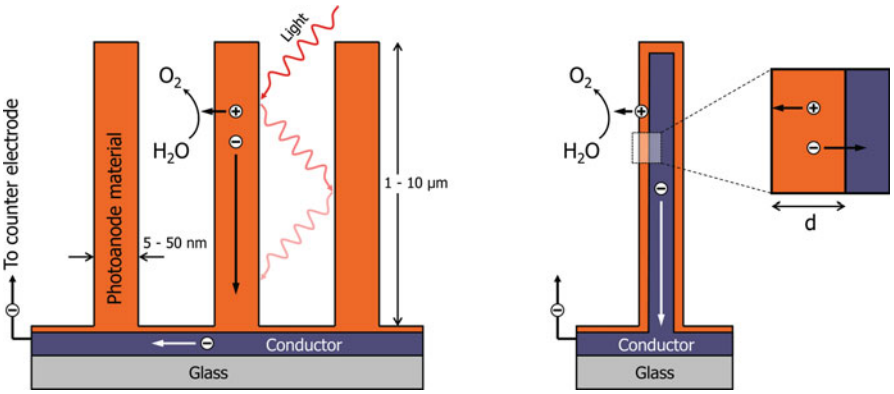

Fig. 2.24 Nanowire array photoanode (*left*), and an array based on highly conducting nanowires coated with a thin photoanode film (*right*)

A third possible advantage of using materials with nanoscale dimensions is the occurrence of quantum size effects. As first described by Brus in the early 1980s, spatial confinement of charge carriers to a volume that is less than their De Broglie wavelength results in a widening of the bandgap [9]. An approximate expression for the bandgap enlargement as a function of particle radius (R) is given by [95]:

$$E_g \simeq E_g^0 + \frac{h^2\pi^2}{2R^2}\left(\frac{1}{m_e^*} + \frac{1}{m_h^*}\right) - \frac{1.8e^2}{\varepsilon_0\varepsilon_r R}. \tag{2.77}$$

Here, E_g^0 is the bulk bandgap and m_e^* and m_h^* are the effective masses for the electrons and holes, respectively. The first term describes the quantum confinement effect, while the second (smaller) term describes the attractive Coulomb interaction between the electrons and holes. The negative sign of the second term shows that it in fact acts against the bandgap enlargement. While the resulting blue shift of the absorption spectrum is usually not desirable for PEC materials, the widening of the gap shifts the conduction band edge positively with respect to the hydrogen reduction energy. This would decrease the required bias potential and increase the solar-to-hydrogen conversion efficiency (2.69) of materials such as α-Fe_2O_3 and WO_3, for which E_C is located below $E^0(H_2/H^+)$ – see Fig. 2.18. Although one recent report claims a 0.3–0.6 eV upward shift of the conduction band of α-Fe_2O_3 nanowires [96], no direct photoelectrochemical evidence for such a shift in α-Fe_2O_3 has been reported so far.

It should be noted that quantum size effects are difficult to induce in most metal oxides. This is due to their relatively large electron and hole effective masses (cf. Table 2.1), which would require exceedingly small particle sizes (<2–3 nm) for any confinement effect to occur. ZnO is a well-known exception that shows appreciable bandgap enlargement at particle sizes below 6 nm [11, 97]. The bandgap

enlargement is generally asymmetric, with $\Delta E_C = h^2\pi^2/(2R^2 m_e^*)$ and $\Delta E_V = h^2\pi^2/(2R^2 m_h^*)$. This asymmetry is less evident in ZnO ($m_e^* = 0.24m_e$, $m_h^* = 0.24m_e$) than in anatase TiO_2 ($m_h^* = 0.8m_e$, $m_e^* = 10m_e$), for which any bandgap enlargement appears to be solely due to a shift in E_V [11]. Clearly, if quantum confinement is to be used to shift the conduction band edge to higher energies without increasing the bandgap too much, one would prefer to have a semiconductor with a small electron effective mass and a large hole effective mass.

An important aspect of nanosized semiconductors is the absence of band bending. Since the number of ionized donors or acceptors in nanosized particles is very small, such particles cannot sustain a large built-in electric field (cf. (2.41) and Fig. 2.13, left). The maximum attainable potential drop within a spherical semiconductor particle with radius R and a donor (or acceptor) density N_D is given by [98]:

$$\phi_{SC} = \frac{-eN_D R^2}{6\varepsilon_0\varepsilon_r}. \tag{2.78}$$

From this expression, the band bending in a 10 nm α-Fe_2O_3 particle ($R = 5$ nm, $\varepsilon_r = 25$) with a relatively high donor density of 10^{18} cm^{-3} is limited to ~3 mV. This clearly shows that the electric field in the space charge of a nanoparticle cannot play a significant role in the separation of photogenerated electrons and holes. Fortunately, most carriers are nevertheless able to reach the interface since the minority carrier diffusion length is – with few exceptions – much larger than the radius of the nanoparticle. As a result, the charge transfer kinetics at the semiconductor/electrolyte interface usually dominate the overall charge separation and recombination kinetics in nanoparticles.

2.9.3 PEC Device Configurations

When the conduction and valence bands do not straddle the water reduction and oxidation potentials, or if the available overpotentials for water splitting are insufficient, a combination of two or more semiconductors may offer a solution. In such a device, one semiconductor acts as a regular photoanode or photocathode. The other semiconductor(s) function(s) as either a complementary photoelectrode, or as an integrated photovoltaic device that provides a bias voltage. Figure 2.25 shows some examples of possible configurations.

Configuration (A) is the one we have used throughout this chapter to illustrate the main principles of photoelectrochemical water splitting. Strontium titanate, $SrTiO_3$, is one of very few materials that have been observed to split water in this configuration [99]. However, the efficiency is less than 1% due to its large bandgap (3.2 eV). Cuprous oxide, Cu_2O, and p-type SiC are candidates for configuration (B). While Cu_2O has been found to suffer from photoreduction to metallic Cu [100, 101],

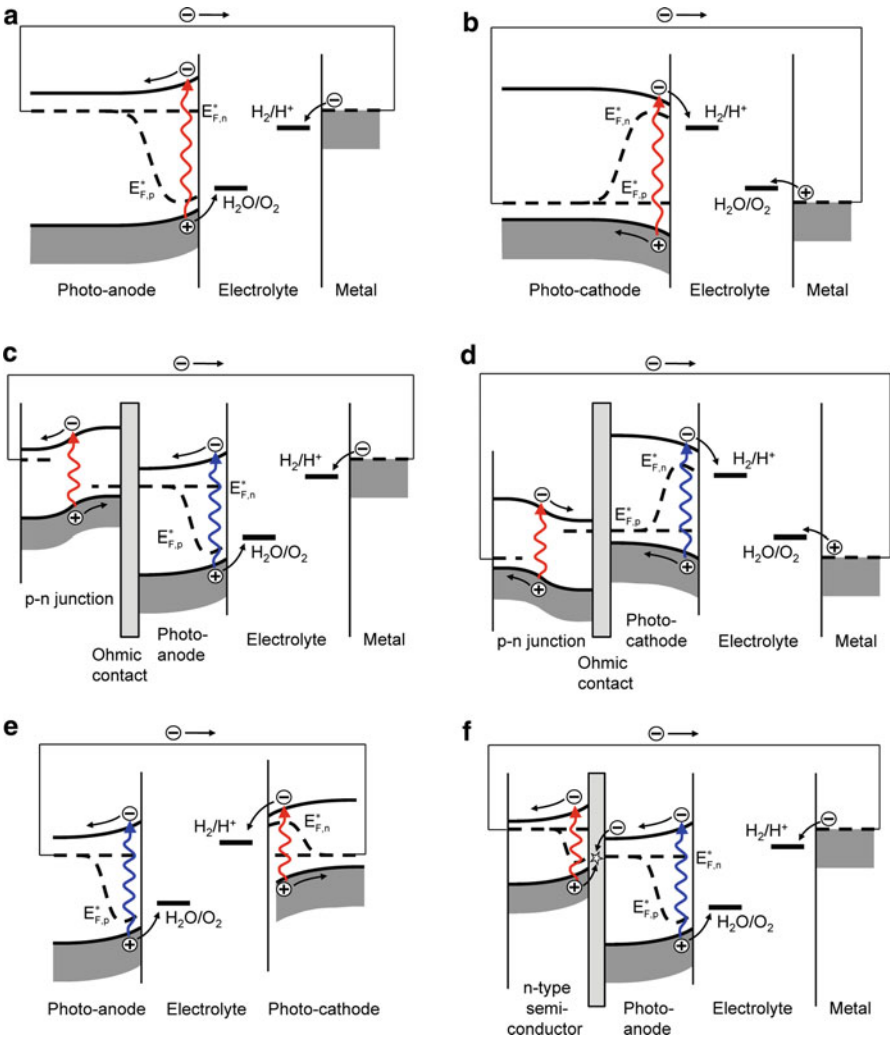

Fig. 2.25 Examples of possible PEC configurations under illumination. *Top row*: Standard single-semiconductor devices based on a photoanode (**a**) or photocathode (**b**) with a metal counter electrode. *Middle row*: Monolithic devices based on a photoanode (**c**) or photocathode (**d**) biased with an integrated p–n junction. *Bottom row*: p–n junction photoelectrochemical device (**e**), and an n–n heterojunction PEC device based on a photoanode deposited on top of a second n-type semiconductor that "boosts" the energy of the electrons (**f**)

other reports indicate that it may be stable under the right conditions [68, 102]. The 4H polytype of silicon carbide is one of the few chemically stable photocathode materials able to split water, but its efficiency is also low ($E_g = 3.26$ eV) [67].

In configurations (C) and (D) a bias voltage is applied to the photoanode and photocathode, respectively, through an integrated p–n junction. Turner et al. have

demonstrated such a monolithic tandem device based on a photocathode of p-type $GaInP_2$ in combination with a GaAs p–n junction [103]. They achieved an impressive solar-to-hydrogen efficiency of 12.4%, but the rapid degradation and high cost of the device limit its practical use. Grätzel and Augustynski used a dye-sensitized solar cell (DSSC) to bias a WO_3 or Fe_2O_3 photoanode [91, 104]. The photoanode absorbs the blue part of the solar spectrum ($E_g = 2.6$ eV for WO_3), whereas the DSSC absorbs red light. This approach is somewhat similar to configuration (C), except for the fact that the p–n junction is replaced by a separate DSSC device. The advantage is that the entire system can be made from low-cost and stable metal oxides. A remaining challenge is to address the significant light scattering of the individual (nanostructured) components, which severely limits the efficiency of the total system [105].

In configurations (E) and (F) an additional bias potential is generated by a single additional absorber instead of a p–n junction. An example of configuration (E) is a device based on n-type TiO_2 ($E_g = 3.2$ eV) and p-type GaP ($E_g = 2.25$ eV) [106]. The difference in bandgaps ensures that a large part of the solar spectrum is used. This is not the case for p–n homojunctions, and devices such as n-Fe_2O_3/p-Fe_2O_3 [107] will not be very efficient because of this. The n–n heterojunction of configuration (F) was first studied many years ago, and was not considered to be very useful since the photogenerated holes in the buried n-type semiconductor could not reach the photoanode/electrolyte interface [108]. More recently, however, Yang et al. showed that n-type Si underneath n-type TiO_2 "boosts" the energy of TiO_2 conduction band electrons [50]. This increases the available overpotential for the reduction of water and improves the kinetics.

Acknowledgments The author gratefully acknowledges Fatwa F. Abdi for critical reading of the manuscript, and the NWO-ACTS Sustainable Hydrogen program (project 053.61.009) and the European Commission's Framework 7 program (NanoPEC, Project 227179) for support.

References

1. Chelikowsky, J.R., Cohen, M.L.: Electronic-structure of silicon. Phys. Rev. B **10**, 5095–5107 (1974)
2. Fujishima, A., Honda, K.: Electrochemical photolysis of water at a semiconductor electrode. Nature **238**, 37–38 (1972)
3. Osterloh, F.E.: Inorganic materials as catalysts for photochemical splitting of water. Chem. Mater. **20**, 35–54 (2008)
4. Stoyanov, E., Langenhorst, F., Steinle-Neumann, G.: The effect of valence state and site geometry on Ti L-3, L-2 and O-K electron energy-loss spectra of Ti_xO_y phases. Am. Miner. **92**, 577–586 (2007)
5. Fischer, D.W.: X-ray band spectra and molecular-orbital structure of rutile TiO_2. Phys. Rev. B **5**, 4219 (1972)
6. Hoffmann, R.: Solids and Surfaces – A Chemist's View of Bonding in Extended Structures. Wiley-VCH, Weinheim (1988)

7. Tauc, J., Grigorov, R., Vancu, A.: Optical properties and electronic structure of amorphous germanium. Phys. Stat. Sol. **15**, 627 (1966)
8. Sze, S.M.: Physics of Semiconductor Devices. Wiley, New York (1981)
9. Brus, L.E.: Electron electron and electron–hole interactions in small semiconductor crystallites – the size dependence of the lowest excited electronic state. J. Chem. Phys. **80**, 4403–4409 (1984)
10. Deskins, N.A., Dupuis, M.: Intrinsic hole migration rates in TiO_2 from density functional theory. J. Phys. Chem. C **113**, 346–358 (2009)
11. Enright, B., Fitzmaurice, D.: Spectroscopic determination of electron and hole effective masses in a nanocrystalline semiconductor film. J. Phys. Chem. **100**, 1027–1035 (1996)
12. Berak, J.M., Sienko, M.J.: Effect of oxygen-deficiency on electrical transport properties of tungsten trioxide crystals. J. Solid State Chem. **2**, 109–133 (1970)
13. Bosman, A.J., Vandaal, H.J.: Small-polaron versus band conduction in some transition-metal oxides. Adv. Phys. **19**, 1 (1970)
14. Matsuzaki, K., Nomura, K., Yanagi, H., Kamiya, T., Hirano, M., Hosono, H.: Epitaxial growth of high mobility Cu_2O thin films and application to p-channel thin film transistor. Appl. Phys. Lett. **93**, 202107 (2008)
15. Kawazoe, H., Yasukawa, M., Hyodo, H., Kurita, M., Yanagi, H., Hosono, H.: P-type electrical conduction in transparent thin films of $CuAlO_2$. Nature **389**, 939–942 (1997)
16. Kudo, A., Yanagi, H., Hosono, H., Kawazoe, H.: $SrCu_2O_2$: a p-type conductive oxide with wide band gap. Appl. Phys. Lett. **73**, 220–222 (1998)
17. Bessekhouad, Y., Gabes, Y., Bouguelia, A., Trari, M.: The physical and photo electrochemical characterization of the crednerite $CuMnO_2$. J. Mater. Sci. **42**, 6469–6476 (2007)
18. Pierret, R.F.: Advanced semiconductor fundamentals. Addison-Wesley, Reading (1989)
19. Asahi, R., Morikawa, T., Ohwaki, T., Aoki, K., Taga, Y.: Photocatalysts sensitive to visible light – response. Science **295**, 627–627 (2002)
20. Maruska, H.P., Ghosh, A.K.: Transition-metal dopants for extending the response of titanate photoelectrolysis anodes. Solar Energy Mater. **1**, 237–247 (1979)
21. Salvador, P.: Analysis of the physical properties of TiO_2-Be electrodes in the photoassisted oxidation of water. Solar Energy Mater. **6**, 241–250 (1982)
22. Henrich, V.E., Cox, P.A.: The surface science of metal oxides. Cambridge University Press, Cambridge (1994)
23. Kato, H., Kudo, A.: Visible-light-response and photocatalytic activities of TiO_2 and $SrTiO_3$ photocatalysts codoped with antimony and chromium. J. Phys. Chem. B **106**, 5029–5034 (2002)
24. Howe, A.T., Hawkins II, R.T., Fleisch, T.H.: Photoelectrochemical cells of the electrolyte–metal–insulator–semiconductor (EMIS) configuration. I. Metal thickness and coverage effects in the Pt/silicon oxide/n-Si system. J. Electrochem. Soc. **133**, 1369–1375 (1986)
25. Piazza, F., Pavesi, L., Henini, M., Johnston, D.: Effect of as overpressure on Si-doped (111) a gaas grown by molecular-beam epitaxy – a photoluminescence study. Semicond. Sci. Technol. **7**, 1504–1507 (1992)
26. Kröger, F.A.: The chemistry of imperfect crystals. North-Holland Publishing Co., Amsterdam (1964)
27. Chiang, Y.-M., Birnie III, D., Kingery, D.W.: Physical Ceramics. Wiley, New York (1997)
28. Smyth, D.M.: The Defect Chemistry of Metal Oxides. Oxford University Press, New York (2000)
29. Jorand Sartoretti, C., Alexander, B.D., Solarska, R., Rutkowska, W.A., Augustynski, J., Cerny, R.: Photoelectrochemical oxidation of water at transparent ferric oxide film electrodes. J. Phys. Chem. B **109**, 13685–13692 (2005)
30. Liang, Y., Enache, C.S., Van de Krol, R.: Photoelectrochemical characterization of sprayed α-Fe_2O_3 thin films: Influence of Si-doping and SnO_2 interfacial layer. Int. J. Photoenergy (2008). doi:10.1155/2008/739864

31. Kennedy, J.H., Shinar, R., Ziegler, J.P.: Alpha-Fe_2O_3 photoanodes doped with silicon. J. Electrochem. Soc. **127**, 2307–2309 (1980)
32. Liang, Y., Tsubota, T., Mooij, L.P.A., van de Krol, R.: Highly improved quantum efficiencies for thin film $BiVO_4$ photoanodes. J. Phys. Chem. C **115**, 17594–17598 (2011)
33. Das Mulmi, D., Sekiya, T., Kamiya, N., Kurita, S., Murakami, Y., Kodaira, T.: Optical and electric properties of Nb-doped anatase TiO_2 single crystal. J. Phys. Chem. Solids **65**, 1181–1185 (2004)
34. Anpo, M., Takeuchi, M.: The design and development of highly reactive titanium oxide photocatalysts operating under visible light irradiation. J. Catal. **216**, 505–516 (2003)
35. Kudo, A., Ueda, K., Kato, H., Mikami, I.: Photocatalytic O_2 evolution under visible light irradiation on $BiVO_4$ in aqueous $AgNO_3$ solution. Catal. Lett. **53**, 229–230 (1998)
36. Sayama, K., Nomura, A., Arai, T., Sugita, T., Abe, R., Yanagida, M., Oi, T., Iwasaki, Y., Abe, Y., Sugihara, H.: Photoelectrochemical decomposition of water into H_2 and O_2 on porous $BiVO_4$ thin-film electrodes under visible light and significant effect of Ag ion treatment. J. Phys. Chem. B **110**, 11352–11360 (2006)
37. Pierret, R.F.: Semiconductor Device Fundamentals. Addison Wesley, Reading (1996)
38. Nicollian, E.H., Brews, J.R.: MOS (metal oxide semiconductor) Physics and Technology. Wiley, Hoboken (2003)
39. Onari, S., Arai, T., Kudo, K.: Ir lattice-vibrations and dielectric-dispersion in alpha-Fe_2O_3. Phys. Rev. B **16**, 1717–1721 (1977)
40. Rosso, K.M., Smith, D.M.A., Dupuis, M.: An ab initio model of electron transport in hematite (alpha-Fe_2O_3) basal planes. J. Chem. Phys. **118**, 6455–6466 (2003)
41. Morrison, S.R.: Electrochemistry of semiconductor and oxidized metal electrodes. Plenum, New York (1980)
42. Bockris, J.O.M., Reddy, A.K.N., Galboa-Aldeco, M.E.: Modern Electrochemistry 2A – Fundamentals of Electrodics. Springer, New York (2001)
43. Memming, R.: Semiconductor Electrochemistry. Wiley, New York (2000)
44. McNaught, A.D., Wilkinson, A.: IUPAC Compendium of Chemical Terminology, 2nd edn. (the "Gold Book"). Blackwell Scientific Publications, Oxford (1997). http://goldbook.iupac.org/S05917.html. Accessed 8 Sep 2010
45. Reichman, J.: The current–voltage characteristics of semiconductor-electrolyte junction photo-voltaic cells. Appl. Phys. Lett. **36**, 574–577 (1980)
46. Peter, L.M., Li, J., Peat, R.: Surface recombination at semiconductor electrodes. 1. Transient and steady-state photocurrents. J. Electroanal. Chem. **165**, 29–40 (1984)
47. Gandia, J., Pujadas, M., Salvador, P.: Electrolyte electroreflectance – easy and reliable flat-band potential measurements. J. Electroanal. Chem. **244**, 69–79 (1988)
48. Radecka, M., Sobas, P., Wimbicka, M., Rekas, M.: Photoelectrochemical properties of undoped and Ti-doped WO_3. Phys. B Condens. Matter **364**, 85–92 (2005)
49. Hagfeldt, A., Björksten, U., Grätzel, M.: Photocapacitance of nanocrystalline oxide semiconductor films: band-edge movement in mesoporous TiO_2 electrodes during UV illumination. J. Phys. Chem. **100**, 8045–8048 (1996)
50. Hwang, Y.J., Boukai, A., Yang, P.D.: High density n-Si/n-TiO_2 core/shell nanowire arrays with enhanced photoactivity. Nano Lett. **9**, 410–415 (2009)
51. Marcus, R.A.: Theory of oxidation–reduction reactions involving electron transfer 1. J. Chem. Phys. **24**, 966–978 (1956)
52. Marcus, R.A.: Chemical + electrochemical electron-transfer theory. Ann. Rev. Phys. Chem. **15**, 155 (1964)
53. Gerischer, H.: Charge transfer processes at semiconductor-electrolyte interfaces in connection with problems of catalysis. Surf. Sci. **18**, 97 (1969)
54. Duret, A., Grätzel, M.: Visible light-induced water oxidation on mesoscopic alpha-Fe_2O_3 films made by ultrasonic spray pyrolysis. J. Phys. Chem. B **109**, 17184–17191 (2005)
55. Jarrett, H.S.: Photocurrent conversion efficiency in a Schottky-barrier. J. Appl. Phys. **52**, 4681–4689 (1981)

56. Wilson, R.H.: Model for current–voltage curve of photoexcited semiconductor electrodes. J. Appl. Phys. **48**, 4292–4297 (1977)
57. Salvador, P.: Kinetic approach to the photocurrent transients in water photoelectrolysis at n-TiO_2 electrodes. I. Analysis of the ratio of the instantaneous to steady-state photocurrent. J. Phys. Chem. **89**, 3863–3869 (1985)
58. Kisumi, T., Tsujiko, A., Murakoshi, K., Nakato, Y.: Crystal-face and illumination intensity dependences of the quantum efficiency of photoelectrochemical etching, in relation to those of water photooxidation, at n-TiO_2 (rutile) semiconductor electrodes. J. Electroanal. Chem. **545**, 99–107 (2003)
59. Imanishi, A., Okamura, T., Ohashi, N., Nakamura, R., Nakato, Y.: Mechanism of water photooxidation reaction at atomically flat TiO_2 (rutile) (110) and (100) surfaces: dependence on solution pH. J. Am. Chem. Soc. **129**, 11569–11578 (2007)
60. Rossmeisl, J., Qu, Z.W., Zhu, H., Kroes, G.J., Norskov, J.K.: Electrolysis of water on oxide surfaces. J. Electroanal. Chem. **607**, 83–89 (2007)
61. Valdes, A., Qu, Z.W., Kroes, G.J., Rossmeisl, J., Norskov, J.K.: Oxidation and photo-oxidation of water on TiO_2 surface. J. Phys. Chem. C **112**, 9872–9879 (2008)
62. Valdes, A., Kroes, G.J.: First principles study of the photo-oxidation of water on tungsten trioxide (WO_3). J. Chem. Phys. **130**(11), 114701 (2009)
63. Harriman, A., Pickering, I.J., Thomas, J.M., Christensen, P.A.: Metal-oxides as heterogeneous catalysts for oxygen evolution under photochemical conditions. J. Chem. Soc. Faraday Trans. I **84**, 2795–2806 (1988)
64. Kanan, M.W., Nocera, D.G.: In situ formation of an oxygen-evolving catalyst in neutral water containing phosphate and Co^{2+}. Science **321**, 1072–1075 (2008)
65. Jiao, F., Frei, H.: Nanostructured cobalt oxide clusters in mesoporous silica as efficient oxygen-evolving catalysts. Angew. Chem. Int. Ed. **48**, 1841–1844 (2009)
66. Kay, A., Cesar, I., Grätzel, M.: New benchmark for water photooxidation by nanostructured alpha-Fe_2O_3 films. J. Am. Chem. Soc. **128**, 15714–15721 (2006)
67. Van Dorp, D.H., Hijnen, N., Di Vece, M., Kelly, J.J.: SiC: a photocathode for water splitting and hydrogen storage. Angew. Chem. Int. Ed. **48**, 6085–6088 (2009)
68. De Jongh, P.E., Vanmaekelbergh, D., Kelly, J.J.: Photoelectrochemistry of electrodeposited Cu_2O. J. Electrochem. Soc. **147**, 486–489 (2000)
69. Rajeshwar, K., McConnell, R., Licht, S.: Solar hydrogen generation – toward a renewable energy future. Springer, New York (2008)
70. Bak, T., Nowotny, J., Rekas, M., Sorrell, C.C.: Photo-electrochemical hydrogen generation from water using solar energy. Materials-related aspects. Int. J. Hydrogen Energy **27**, 991–1022 (2002)
71. Park, S.M., Barber, M.E.: Thermodynamic stabilities of semiconductor electrodes. J. Electroanal. Chem. **99**, 67–75 (1979)
72. Scaife, D.E.: Oxide semiconductors in photoelectrochemical conversion of solar energy. Solar Energy **25**, 41–54 (1980)
73. Kudo, A., Miseki, Y.: Heterogeneous photocatalyst materials for water splitting. Chem. Soc. Rev. **38**, 253–278 (2009)
74. Ritterskamp, P., Kuklya, A., Wustkamp, M.A., Kerpen, K., Weidenthaler, C., Demuth, M.: A titanium disilicide derived semiconducting catalyst for water splitting under solar radiation – reversible storage of oxygen and hydrogen. Angew. Chem. Int. Ed. **46**, 7770–7774 (2007)
75. Solar Irradiance Data, ASTM-G173-03 (AM1.5, global tilt): http://rredc.nrel.gov/solar/spectra/am1.5/. Accessed 11 Aug 2010
76. Chen, Z.B., Jaramillo, T.F., Deutsch, T.G., Kleiman-Shwarsctein, A., Forman, A.J., Gaillard, N., Garland, R., Takanabe, K., Heske, C., Sunkara, M., McFarland, E.W., Domen, K., Miller, E.L., Turner, J.A., Dinh, H.N.: Accelerating materials development for photoelectrochemical hydrogen production: standards for methods, definitions, and reporting protocols. J. Mater. Res. **25**, 3–16 (2010)

77. Murphy, A.B., Barnes, P.R.F., Randeniya, L.K., Plumb, I.C., Grey, I.E., Horne, M.D., Glasscock, J.A.: Efficiency of solar water splitting using semiconductor electrodes. Int. J. Hydrogen Energy **31**, 1999–2017 (2006)
78. Santato, C., Ulmann, M., Augustynski, J.: Enhanced visible light conversion efficiency using nanocrystalline WO_3 films. Adv. Mater. **13**, 511 (2001)
79. Kavan, L., Grätzel, M.: Highly efficient semiconducting TiO_2 photoelectrodes prepared by aerosol pyrolysis. Electrochim. Acta **40**, 643–652 (1995)
80. De Jongh, P.E., Vanmaekelbergh, D.: Trap-limited electronic transport in assemblies of nanometer-size TiO_2 particles. Phys. Rev. Lett. **77**, 3427–3430 (1996)
81. Van de Krol, R., Liang, Y.Q., Schoonman, J.: Solar hydrogen production with nanostructured metal oxides. J. Mater. Chem. **18**, 2311–2320 (2008)
82. Weber, M.F., Dignam, M.J.: Splitting water with semiconducting photoelectrodes efficiency considerations. Int. J. Hydrogen Energy **11**, 225–232 (1986)
83. Bolton, J.R., Strickler, S.J., Connolly, J.S.: Limiting and realizable efficiencies of solar photolysis of water. Nature **316**, 495–500 (1985)
84. Gerischer, H.: Electrochemical behavior of semiconductors under illumination. J. Electrochem. Soc. **113**, 1174 (1966)
85. Weber, M.F., Dignam, M.J.: Efficiency of splitting water with semiconducting photoelectrodes. J. Electrochem. Soc. **131**, 1258–1265 (1984)
86. Liang, Y., Enache, C.S., Van de Krol, R.: Photoelectrochemical characterization of sprayed α-Fe_2O_3 thin films: Influence of Si-doping and SnO_2 interfacial layer. Int. J. Photoenergy (2008). doi:10.1155/2008/739864
87. Licht, S., Wang, B., Mukerji, S., Soga, T., Umeno, M., Tributsch, H.: Efficient solar water splitting, exemplified by RuO_2-catalyzed AlGaAs/Si photoelectrolysis. J. Phys. Chem. B **104**, 8920–8924 (2000)
88. Youngblood, W.J., Lee, S.H.A., Kobayashi, Y., Hernandez-Pagan, E.A., Hoertz, P.G., Moore, T.A., Moore, A.L., Gust, D., Mallouk, T.E.: Photoassisted overall water splitting in a visible light-absorbing dye-sensitized photoelectrochemical cell. J. Am. Chem. Soc. **131**, 926 (2009)
89. Maeda, K., Teramura, K., Lu, D.L., Takata, T., Saito, N., Inoue, Y., Domen, K.: Photocatalyst releasing hydrogen from water – enhancing catalytic performance holds promise for hydrogen production by water splitting in sunlight. Nature **440**, 295–295 (2006)
90. Kato, H., Asakura, K., Kudo, A.: Highly efficient water splitting into H_2 and O_2 over lanthanum-doped $NaTaO_3$ photocatalysts with high crystallinity and surface nanostructure. J. Am. Chem. Soc. **125**, 3082–3089 (2003)
91. Grätzel, M.: Photoelectrochemical cells. Nature **414**, 338–344 (2001)
92. Mor, G.K., Prakasam, H.E., Varghese, O.K., Shankar, K., Grimes, C.A.: Vertically oriented Ti-Fe-O nanotube array films: toward a useful material architecture for solar spectrum water photoelectrolysis. Nano Lett. **7**, 2356–2364 (2007)
93. Sivula, K., Le Formal, F., Grätzel, M.: WO_3–Fe_2O_3 photoanodes for water splitting: a host scaffold guest absorber approach. Chem. Mater. **21**, 2862–2867 (2009)
94. Cesar, I., Kay, A., Martinez, J.A.G., Grätzel, M.: Translucent thin film Fe_2O_3 photoanodes for efficient water splitting by sunlight: nanostructure-directing effect of Si-doping. J. Am. Chem. Soc. **128**, 4582–4583 (2006)
95. Brus, L.: Electronic wave-functions in semiconductor clusters – experiment and theory. J. Phys. Chem. **90**, 2555–2560 (1986)
96. Vayssieres, L., Sathe, C., Butorin, S.M., Shuh, D.K., Nordgren, J., Guo, J.H.: One-dimensional quantum-confinement effect in alpha-Fe_2O_3 ultrafine nanorod arrays. Adv. Mater. **17**, 2320 (2005)
97. Lin, K.F., Cheng, H.M., Hsu, H.C., Lin, L.J., Hsieh, W.F.: Band gap variation of size-controlled ZnO quantum dots synthesized by sol-gel method. Chem. Phys. Lett. **409**, 208–211 (2005)

98. Goossens, A.: Potential distribution in semiconductor particles. J. Electrochem. Soc. **143**, L131–L133 (1996)
99. Mavroides, J.G., Kafalas, J.A., Kolesar, D.F.: Photoelectrolysis of water in cells with $SrTiO_3$ anodes. Appl. Phys. Lett. **28**, 241–243 (1976)
100. Schoppel, H.R., Gerischer, H.: Cathodic reduction of Cu-I oxide electrodes as example for reduction mechanism of semiconductor crystal. Ber. Bunsenges. Phys. Chem. **75**, 1237 (1971)
101. Nagasubramanian, G., Gioda, A.S., Bard, A.J.: Semiconductor electrodes. 37. Photoelectrochemical behavior of p-type Cu_2O in acetonitrile solutions. J. Electrochem. Soc. **128**, 2158–2164 (1981)
102. Hara, M., Kondo, T., Komoda, M., Ikeda, S., Shinohara, K., Tanaka, A., Kondo, J.N., Domen, K.: Cu_2O as a photocatalyst for overall water splitting under visible light irradiation. Chem. Commun. **3**, 357–358 (1998)
103. Khaselev, O., Turner, J.A.: A monolithic photovoltaic-photoelectrochemical device for hydrogen production via water splitting. Science **280**, 425–427 (1998)
104. Grätzel, M.: Mesoscopic solar cells for electricity and hydrogen production from sunlight. Chem. Lett. **34**, 8–13 (2005)
105. Brillet, J., Cornuz, M., Le Formal, F., Yum, J.H., Grätzel, M., Sivula, K.: Examining architectures of photoanode-photovoltaic tandem cells for solar water splitting. J. Mater. Res. **25**, 17–24 (2010)
106. Nozik, A.J.: p–n photoelectrolysis cells. Appl. Phys. Lett. **29**, 150–153 (1976)
107. Turner, J.E., Hendewerk, M., Somorjai, G.A.: The photodissociation of water by doped iron-oxides – the unbiased P/N assembly. Chem. Phys. Lett. **105**, 581–585 (1984)
108. Kohl, P.A., Frank, S.N., Bard, A.J.: Semiconductor electrodes. 11. Behavior of n-type and p-type single-crystal semiconductors covered with thin normal-TiO_2 films. J. Electrochem. Soc. **124**, 225–229 (1977)

http://www.springer.com/978-1-4614-1379-0

Photoelectrochemical Hydrogen Production
van de Krol, R.; Grätzel, M. (Eds.)
2012, VIII, 324 p., Hardcover
ISBN: 978-1-4614-1379-0